

Using a reactive transport model to elucidate differences between laboratory and field dissolution rates in regolith

Joel Moore^{a,b,*}, Peter C. Lichtner^c, Art F. White^d, Susan L. Brantley^{a,b}

^a Department of Geosciences, Penn State University, University Park, PA, United States

^b Center for Environmental Kinetics Analysis, Earth and Environmental Systems Institute, Penn State University, University Park, PA, United States

^c Los Alamos National Laboratory, Los Alamos, NM, United States

^d US Geological Survey, Menlo Park, CA, United States

Received 18 October 2010; accepted in revised form 14 March 2012; available online 24 March 2012

Abstract

The reactive transport model FLOTRAN was used to forward-model weathering profiles developed on granitic outwash alluvium over 40–3000 ka from the Merced, California (USA) chronosequence as well as deep granitic regolith developed over 800 ka near Davis Run, Virginia (USA). Baseline model predictions that used laboratory rate constants (k_m), measured fluid flow velocities (v), and BET volumetric surface areas for the parent material ($A_{B,m}^o$) were not consistent with measured profiles of plagioclase, potassium feldspar, and quartz. Reaction fronts predicted by the baseline model are deeper and thinner than the observed, consistent with faster rates of reaction in the model. Reaction front depth in the model depended mostly upon saturated versus unsaturated hydrologic flow conditions, rate constants controlling precipitation of secondary minerals, and the average fluid flow velocity (v_a). Unsaturated hydrologic flow conditions (relatively open with respect to $\text{CO}_{2(g)}$) resulted in the prediction of deeper reaction fronts and significant differences in the separation between plagioclase and potassium feldspar reaction fronts compared to saturated hydrologic flow (relatively closed with respect to $\text{CO}_{2(g)}$). Under saturated or unsaturated flow conditions, the rate constant that controls precipitation rates of secondary minerals must be reduced relative to laboratory rate constants to match observed reaction front depths and measured pore water chemistry. Additionally, to match the observed reaction front depths, v_a was set lower than the measured value, v , for three of the four profiles. The reaction front gradients in mineralogy and pore fluid chemistry could only be modeled accurately by adjusting values of the product $k_m A_{B,m}^o$. By assuming k_m values were constrained by laboratory data, field observations were modeled successfully with TST-like rate equations by dividing measured values of $A_{B,m}^o$ by factors from 50 to 1700. Alternately, with sigmoidal or Al-inhibition rate models, this adjustment factor ranges from 5 to 170. Best-fit models of the wetter, hydrologically saturated Davis Run profile required a smaller adjustment to $A_{B,m}^o$ than the drier hydrologically unsaturated Merced profiles. We attributed the need for large adjustments in v_a and $A_{B,m}^o$ necessary for the Merced models to more complex hydrologic flow that decreased the reactive surface area in contact with bulk flow water, e.g., dead-end pore spaces containing fluids that are near or at chemical equilibrium. Thus, rate models from the laboratory can successfully predict weathering over millions of years, but work is needed to understand how to incorporate changes in what controls the relationship between reactive surface area and hydrologic flow.

© 2012 Elsevier Ltd. All rights reserved.

1. INTRODUCTION

* Corresponding author. Present Address: Dept. of Physics, Astronomy, and Geosciences, Towson University, Towson, MD, United States.

E-mail address: joelmoore6@gmail.com (J. Moore).

Silicate mineral weathering yields nutrients to ecosystems (e.g., Carey et al., 2005), buffers acid deposition (e.g., Williams and Melack, 1997), and contributes elemental

fluxes to the ocean (e.g., Kump et al., 2000). On the million-year time scale, silicate mineral weathering is one of the major sinks for atmospheric CO₂ (e.g., Berner, 1995). The ability to successfully model mineral dissolution in soils will be important for predicting how variations in temperature and precipitation due to global climate change will affect soil chemistry into the future (e.g., Williams et al., 2003). Predictions of mineral dissolution rates are also necessary to understand numerous other societal issues including maintenance of water quality (e.g., Malmström et al., 2000), nuclear waste disposal (e.g., Yokoyama et al., 2005), and geologic carbon sequestration (e.g., Carroll and Knauss, 2005). However, researchers find that mineral dissolution rates calculated from field data, including rates calculated from aquifers, soil pore waters, soil chemistry, and stream chemistry, are two to five orders of magnitude slower than experimental mineral dissolution rates observed under far-from-equilibrium conditions (e.g., White et al., 1996; Oliva et al., 2003; White et al., 2005; Zhu, 2005; White et al., 2008). The large differences in rates make it difficult to predict mineral dissolution in field systems using experimental data.

Chemical, physical, and biological factors all contribute to the observed differences between laboratory and field dissolution rates (White and Brantley, 2003). Some chemical and physical factors seem to be intrinsic to the mineral substrates themselves. By careful choice of mineral substrates for dissolution in the laboratory, these chemical and mineralogical factors can be minimized between laboratory and field as well as between field sites (White and Brantley, 2003). Chemical composition and mineralogical structure are clearly intrinsic factors that affect mineral reactivity. For example, exsolution lamellae are common to feldspar and affect reactivity such that calcic zones dissolve more quickly than sodic zones (e.g., Oliva et al., 2004; White et al., 2008). Another common factor is that certain minerals have higher specific surface area, e.g., plagioclase has a higher specific surface area than quartz, which may indicate higher reactivity.

However, some of these “intrinsic factors” vary over long time intervals and are therefore hard to measure in the laboratory. For example, reactive surface area diminishes over time (White et al., 1996; White and Brantley, 2003) and with the approach to chemical equilibrium, which itself varies with time and position (Shiraki and Brantley, 1995; Beig and Lutge, 2006). In contrast, BET surface area increases with dissolution duration (White et al., 1996; Hodson et al., 1998). Additionally, the rate equation for a given mineral could be considered an intrinsic factor, particularly when the rates are based on conditions typically found in the field. For example, rate equations describe how dissolution is promoted or inhibited by aqueous species, e.g., alkali feldspar dissolution can be inhibited by aqueous Al³⁺ (Oelkers et al., 1994; Stillings et al., 1996). Likewise, each mineral can be characterized with respect to how its dissolution rate varies with chemical affinity, e.g., plagioclase dissolution rates non-linearly decrease as chemical equilibrium is approached (e.g., Burch et al., 1993; Hellmann and Tisserand, 2006). Similarly, rates of secondary mineral precipitation slow near equilibrium, a

phenomena that has been observed in laboratory experiments (e.g., Yang and Steefel, 2008; Zhu and Lu, 2009) but only suggested in field studies due to difficulty of measurement (e.g., Zhu et al., 2004; Godderis et al., 2006; Maher et al., 2009).

Characteristics that are clearly external to the minerals themselves are referred to as extrinsic factors. These factors, predominantly physical and biological in nature, vary between laboratory and field and among field sites. Perhaps the key physical extrinsic factor is hydrology, which includes the amount of water flowing through a system as well as the hydrological heterogeneity. Heterogeneity results in regions with differing rates of advection as well as regions of low or no permeability (e.g., dead end pores or micropores) where diffusive transport dominates (Green et al., 2005; White et al., 2005; Evans and Banwart, 2006). Biological extrinsic factors are related to ecosystem functions. For example, plants and microorganisms take up water and inorganic nutrients such as Ca, K, and P (Crews et al., 1995; Bormann et al., 1998; Moulton et al., 2000). Plants and fungi produce organic matter and organic acids that can play a direct role in mineral dissolution (Stillings et al., 1996; Drever and Stillings, 1997) as well as in transport of Al and Fe from the surface soil to subsurface horizons (Lundström et al., 2000; Masiello et al., 2004). Plants slow physical erosion by holding soil particles in place with root systems (Drever, 1994). These extrinsic factors are difficult to investigate in the laboratory.

The combination of ideal field sites and a reactive transport model gives the opportunity to determine the role that these intrinsic and extrinsic factors play in driving the difference between laboratory and field dissolution rates. We selected two field sites where field weathering rates of plagioclase and potassium feldspar (*k*-feldspar) are 3–4 orders of magnitude slower (White et al., 1996; White et al., 2001; White et al., 2005) than far-from-equilibrium laboratory rates for feldspar dissolution under similar pH conditions (Bandstra and Brantley, 2008). To investigate weathering at these sites, FLOTTRAN, a coupled chemical and hydrological reactive transport model (Lichtner, 2007), was used to forward-model dissolution of the parent material over millions of years. Using FLOTTRAN, we systematically evaluated many of the chemical and physical factors that control feldspar dissolution and contribute to the large difference between laboratory and field dissolution rates.

2. SITE DESCRIPTION AND FIELD DATA

The two granitic weathering sites we investigated included: (1) several soil profiles from a granitic alluvial chronosequence (durations of soil formation from 40 to 3000 ka) along the Merced River, California, USA, and (2) the Davis Run granitic regolith in Virginia, USA (soil residence time estimated to equal 800 ka). Davis Run provided a contrast to Merced in that it weathered under a cooler and wetter climate, experienced higher and more constant values of water saturation, and is a deeper weathering profile developed on bedrock. Dissolution of plagioclase feldspar, the most abundant mineral in both settings, is the most important dissolution reaction in terms

of elemental fluxes. Dissolution of plagioclase feldspar, potassium feldspar (*k*-feldspar), and quartz, as well as precipitation of kaolinite, are modeled at both sites.

2.1. Merced

The Merced chronosequence soils, formed on dissected terraces along the Merced River in the eastern Central Valley and western foothills of the Sierra Nevada in California (USA), have been the subject of extensive study for temporal trends in pedology, soil mineral weathering, soil pore water chemistry, ecology, and hydrology (Harden, 1982; Pavich et al., 1986; Harden, 1987; White et al., 1996; Baisden et al., 2002; Bullen et al., 2004; Green et al., 2005; White et al., 2005). We focus on soils formed on the lower member of the Modesto formation (duration of soil formation = 40 ka), the middle member of the Riverbank formation (250 ka), the Turlock Lake formation (600 ka), and the China Hat formation (3000 ka). The three older soils are within 10 km of each other and the 40 ka soil is within 20 km (White et al., 1996). The soils formed on a parent material of reworked alluvial sediments dominantly derived from granitic rocks in the interior of the Sierra Nevada (Harden, 1987). Erosion is assumed minimal for Merced soils as described previously (Pavich et al., 1986; White et al., 1996). Therefore, depletion of primary minerals is attributed to mineral dissolution rather than physical erosion. Merced chronosequence soils younger than 40 ka are not modeled because the younger soils also include minerals derived from metamorphic rocks located in the foothills of the Sierra Nevada (Harden, 1987) and depositional effects result in considerable variation in mineral composition. Mean annual temperature (MAT) and precipitation (MAP) from 1930 to 2003 at Turlock Lake (~40 km distant) are 16 °C and 30.6 cm, respectively (Harden, 1987; White et al., 2005).

Plagioclase, quartz, and *k*-feldspar are the most common minerals in the parent material with lesser hornblende and biotite (White et al., 1996). The clay fraction (<4 μm) is predominantly kaolinite in all soils (White et al., 1996). For the 250, 600, and 3000 ka terraces, data from multiple depth profiles were reported (Harden, 1987; White et al., 1996). Primary mineral concentrations in the sand and silt fractions from each profile were measured by quantitative X-ray diffraction (Table EA-1). The concentration profiles were used to construct a depth-weighted average profile for each terrace (Appendix A).

The fractional depletion or enrichment of component *j* relative to the parent material after correction for relative enrichment or depletion of other mobile components can be calculated as:

$$\tau_{j,i} = \frac{C_j C_i^o}{C_j^o C_i} - 1 \quad (1)$$

Here $\tau_{j,i}$ is the mass transfer coefficient for *j* at a given depth, C_j and C_j^o are the concentration (g g⁻¹ or m³ m⁻³ regolith) of *j* in the weathering and parent material, respectively, and C_i and C_i^o are the concentrations of immobile components *i* in the weathered and parent material, respectively (e.g., Brimhall et al., 1988; Chadwick et al., 1990;

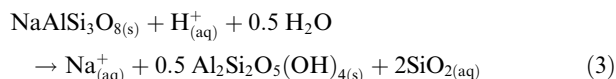
Anderson et al., 2002). Note that Table 1 summarizes a list of symbols. When $\tau_{j,i} = 0$, *j* is neither enriched nor depleted compared to *i*; when $\tau_{j,i} = -1$, *j* is completely depleted; when $\tau_{j,i} > 0$, *j* is enriched relative to *i*. For the Merced soils, we define each component *j* or *i* as a mineral. (In recognition of this, we often use subscript *m* instead of *j* in equations below; see Table 1 for subscripts for specific minerals.) Quartz, *q*, is defined as *i* as in White et al. (1996) because no significant quartz dissolution occurred at Merced through 3000 ka: i.e., relative quartz concentrations increase with soil age as more soluble minerals weather away (White et al., 1996). Additionally, quartz density is similar to plagioclase and *k*-feldspar, reducing variation due to the original alluvial deposition (White et al., 1996).

For *j* defined as mineral *m*, the fraction of *m* that remains in the column from the surface down to the bottom of the profile was calculated as:

$$F_m = \left[1 - \frac{\sum (V_m^o \tau_{j,i} z_x)}{\sum (V_m^o z_x)} \right] (100) \quad (2)$$

where V_m^o is the volume fraction of mineral *m* in the parent material (m³ mineral m⁻³ regolith) and z_x is the thickness of a given sample or model interval *x* (note that the sum over all z_x equals the total weathering depth). Ideally mineral losses over a depth profile are calculated using volume loss or gain in addition to $\tau_{j,i}$ following equations published in the literature (Brantley and Lebedeva, 2011). However, the data to calculate strain were not available for all Merced samples. For the depth interval of the 250 ka soil with the largest reported strain (~28%, calculated using bulk densities listed in Table EA-2), F_m as calculated from Eq. (2) is 57.9%. Using an equation that incorporates strain, Eq. (3) in Brantley and Lebedeva (2011), the value is 69.3%. The difference is smaller for the other depth intervals with lower strain values.

At Merced, $\tau_{plag,q}$ at the surface decreases from -0.35 in the 250 ka soil to -0.50 at 600 ka to -0.95 at 3000 ka (Fig. 1A–C, Table EA-3). In contrast, $\tau_{kf,q}$ equals 0 through 600 ka and then decreases to approximately -0.80 at 3000 ka (Table EA-3). Secondary kaolinite concentrations increase with soil age as primary minerals dissolve and kaolinite precipitates (Fig. 1A–C). Pore water chemistry across the chronosequence reflects the soil mineralogy and chemistry changes (White et al., 2005). A dominant reaction in Merced soils is dissolution of albite (NaAlSi₃O₈) coupled with precipitation of kaolinite (Al₂Si₂O₅(OH)₄):



A similar reaction can be written for *k*-feldspar. While these reactions are written assuming that Al is conservative in the soils, no such assumption is built into FLOTTRAN.

2.2. Davis Run

The Davis Run saprolite is located in Fairfax County, VA and overlies the Occoquan granite, which has been described as foliated granite or gneissic granite (Pavich et al.,

Table 1

List of parameters used in this paper.

Symbol	Definition	Units
A_m	Surface area for a given mineral m	$\text{m}^2 \text{m}^{-3}$
$A_{B,m}^o$	BET surface area for a given mineral m in the parent material	$\text{m}^2 \text{m}^{-3}$
$A_{r,m}^o$	Reactive surface area for a given mineral m in the parent material	$\text{m}^2 \text{m}^{-3}$
β_m	Affinity power	
C_i	Concentration of some immobile component i in the weathering regolith (solid phase)	$\text{m}^3 \text{m}^{-3}$
C_i^o	Concentration of some immobile component i in the parent (solid phase)	$\text{m}^3 \text{m}^{-3}$
C_j	Concentration of some mobile component j in the weathering regolith (solid phase)	$\text{m}^3 \text{m}^{-3}$
C_j^o	Concentration of some mobile component j in the parent (solid phase)	$\text{m}^3 \text{m}^{-3}$
C_{eq}	C_{eq} is the aqueous concentration of an element or molecule at chemical equilibrium with a mineral	mol m^{-3}
C_o	C_o is the aqueous concentration of an element or molecule	mol m^{-3}
F_m	Fraction of some mineral m remaining	$\text{m}^3 \text{m}^{-3}$
H	Hydrologic saturation state where 100% is saturated flow and <100% is unsaturated flow	%
j	Subscript for a mobile component; since mobile components in our system are typically minerals, subscript m is usually substituted for subscript j	
k_m	Dissolution rate constant for mineral m	$\text{mol m}^{-2} \text{s}^{-1}$
k_m^{FFE}	Far-from-equilibrium dissolution rate constant for plagioclase (from empirical fit)	$\text{mol m}^{-2} \text{s}^{-1}$
k_m^{NE}	Near-equilibrium dissolution rate constant for plagioclase (from empirical fit)	$\text{mol m}^{-2} \text{s}^{-1}$
\hat{k}_m	Dissolution rate constant for mineral m	m y^{-1}
K	Equilibrium constant for mineral m with dissolution reaction as forward reaction	
K_m	Equilibrium constant for mineral m with precipitation reaction as forward reaction	
K_p	Equilibrium constant for primary aqueous species	
K_s	Equilibrium constant for secondary aqueous species	
L_j	Slope of reaction front (weathering gradient)	
λ	Exponent for the relationship between surface area and volume	
m	Subscript for a mineral component; specific minerals may be substituted were applicable ($k^f = k$ -feldspar, $kaol$ = kaolinite, $plag$ = plagioclase, q = quartz)	
M_{aq}	Aqueous species in mineral–water reaction	
M_s	Mineral species in mineral–water reaction	
P_m	Prefactor for mineral m	
ρ_m	Density for a given mineral m	g m^{-3}
Q_m	Ion activity product for mineral m	
R_m	Dissolution or precipitation rate for mineral m	$\text{mol m}^{-3} \text{porous medium s}^{-1}$
σ_m	Temkin's constant	
S_m	BET specific surface area	$\text{m}^2 \text{g}^{-1}$
$\tau_{j,i}$	Mass transfer coefficient of weatherable mineral j relative to immobile component i	
$\tau_{j,i}^t$	Mass transfer coefficient at the top of the reaction front	
$\tau_{j,i}^b$	Mass transfer coefficient at the bottom of the reaction front	
v	Field measured Darcy flow velocity	m y^{-1}
v_a	Average flow velocity for a model	m y^{-1}
V_m^o	Volume fraction of some mineral m in the parent material	$\text{m}^3 \text{m}^{-3}$
V_m	Volume fraction of some mineral m (Section 3.5.4)	$\text{m}^3 \text{m}^{-3}$
\bar{V}_m	Molar volume for some mineral m	$\text{m}^3 \text{mol}^{-1}$
ω_m	Advance rate of reaction front	m y^{-1}
z_x	Thickness for some interval x	m
Z_m^t	Top of reaction front. Defined as the depth when mineral concentration = ~0% of parent concentration or a minimum value	m
Z_m^{mid}	Midpoint of reaction front (depth below surface). Defined as the depth where $\tau \approx -0.1$, i.e., the depth where mineral concentration is = 50% of the parent concentration.	m
Z_m^b	Bottom of reaction front (depth below surface). Defined as the depth where $\tau \approx -0.1$, i.e., the depth where mineral concentration is = 90% of the parent concentration	m

1985; Pavich, 1986; Pavich et al., 1989). The landscape is considered to have reached geomorphologic steady state with isovolumetric transformation of bedrock to saprolite occurring at the same rate as the erosion of material from the surface (Pavich, 1986; White et al., 2001). For such a system, the weathering fronts move downward at the same rate that the surface erodes (Pavich, 1986; White et al., 2001). In our modeling we follow a previous weathering study (White et al., 2001) that estimates the regolith resi-

dence time to be 800 ka based on ^{10}Be measurements (Pavich et al., 1985). The MAT at this site is 10 °C and the MAP is 1.04 m (Pavich, 1986).

While no new quantitative mineralogical data were measured for Davis Run, soil and saprolite chemistry were used in combination with published bedrock mineralogy (Seiders et al., 1975) to estimate mineral phase abundance. Like the Merced case study, sodium (Na) in the parent material is found almost exclusively in the albitic plagioclase (An_6 ,

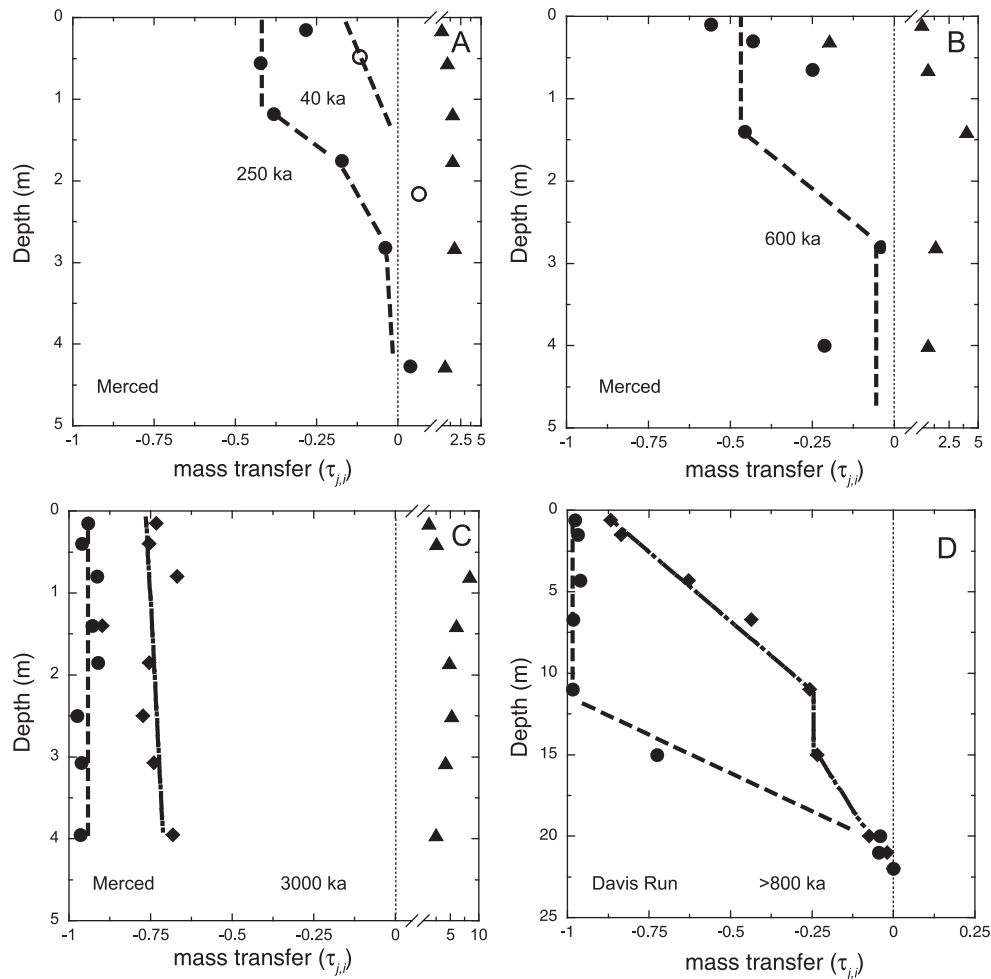


Fig. 1. Mineral abundance versus depth for Merced and Davis Run. Depth versus $\tau_{j,q}$ for j = plagioclase (circles), k -feldspar (diamonds), and kaolinite (triangles) versus depth for (A) Merced soils at 40 ka (open circle) and 250 ka (filled circle), (B) Merced soil at 600 ka, (C) Merced soil at 3000 ka, and (D) Davis Run. Note the different depth scale for Davis Run. Values for $\tau_{j,q} = -1$ when a component is completely depleted relative to the parent material, = 0 when the component concentration is the same as the parent, and > 0 when a component is enriched relative to the parent.

White et al., 2001); therefore, Na concentrations in the saprolite and soil were used as a proxy for plagioclase concentration. Na concentrations are near zero from the surface down to the top of the reaction front (11 m depth). Na then increases to the parent concentration at the bottom of the reaction front (20 m depth, Fig. 1D and Table EA-4).

Potassium (K) concentrations, also depleted at the surface, increase from the surface down to weathered bedrock (Fig. 1D). Depletion of K is attributed largely to dissolution of k -feldspar (White et al., 2001). While K is also present in muscovite, saprolite chemistry indicates muscovite is stable in the saprolite (White et al., 2001). Kaolinite is the dominant secondary phase in the saprolite (Pavich, 1986). We use TiO_2 as the immobile component when calculating $\tau_{j,i}$, for field data following White et al. (2001). However, because we did not include the immobile element Ti in our FLOTTRAN model, for plots of τ from FLOTTRAN, we set i = quartz.

2.3. Key features of the reaction fronts

The depth of the midpoint of a reaction front for a mineral in a profile documents the depth of the weathering advance for that mineral. Front depths plotted versus time for a non-eroding profile such as Merced therefore document the weathering advance rate. The change in mineral concentration plotted versus depth across the reaction front defines the weathering gradient (White, 2002).

In our modeling of Merced, we emphasized the simulation of several key features of the regolith: depths of reaction fronts and weathering gradients for plagioclase and k -feldspar over time; lack of quartz dissolution through 3000 ka; extent of precipitation and gradient for kaolinite; alkalinity, pH, and dissolved concentrations of Na and SiO_2 in pore fluids versus depth and time; and mineral saturation states at 250 ka. At Davis Run, our modeling focused on simulation of the plagioclase reaction front depth and weathering gradient as well as its separation distance

from the k -feldspar reaction front. A secondary goal was to simulate the depth and slope of the k -feldspar reaction front.

3. METHODS AND MODEL INPUTS

3.1. Reaction fronts

A reaction front is defined as the portion of a depth profile over which the concentration of some component decreases from the parent material concentration to some minimum value (Fig. 2, White, 2002; Brantley et al., 2007, 2008). A key feature of reaction fronts is the slope, or weathering gradient. For mineral m , the slope of the reaction front (L_m) is here defined as:

$$L_m = \frac{Z_m^b - Z_m^t}{\tau_{m,i}^b - \tau_{m,i}^t} \quad (4)$$

where Z_m^t and Z_m^b (m) are the depth of the top and bottom of the reaction front, respectively (Fig. 2) and $\tau_{m,i}^t$ and $\tau_{m,i}^b$ are the mass transfer coefficients at the top and bottom of the reaction front, respectively. In our calculations, we defined Z_m^b as the depth where $\tau_{m,i}^b \approx -0.1$ (i.e., the depth where mineral concentration is = 90% of the parent concentration) and Z_m^t as the depth where $\tau_{m,i}^t \approx -1$ or a minimum value in the profile. The slope reveals information about the kinetics of reaction relative to transport (Ortoleva et al., 1986; Lichtner, 1988, 1996; Murphy et al., 1998; White, 2002; Brantley et al., 2008; Brantley and White, 2009).

For an advection-dominated porous column without erosion, when a reaction front is formed for a single mineral m that dissolves to yield a single aqueous species (e.g., quartz to $\text{SiO}_{2(\text{aq})}$), L_m is described by the following equation:

$$L_m = \frac{v_a}{\hat{k}_m A_m} \quad (5a)$$

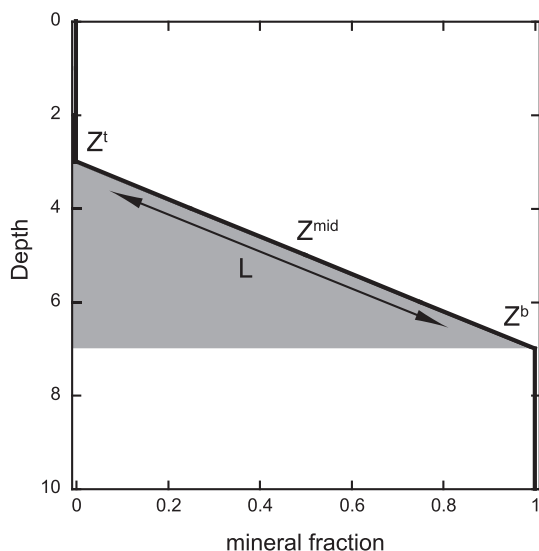


Fig. 2. Depth versus mineral fraction for a schematic reaction front. Depth of the top (Z^t), middle (Z^{mid}), bottom (Z^b), and slope (L) of the reaction front are labeled.

where v_a is the average fluid flow velocity (m y^{-1}), \hat{k}_m is the dissolution rate constant for mineral m (m y^{-1}), and A_m is volumetric surface area for mineral m ($\text{m}^2 \text{m}^{-3}$) (for more details see Lichtner, 1988, 1996, 1998). Additionally, Eq. (5a) assumes a constant mineral surface area. Eq. (5a) demonstrates how variations in v_a or $\hat{k}_m A_m$ control L_m . Although Eq. (5a) was derived for single-component, single-phase systems that are not eroding, it has been shown to be useful for conceptualizing more complex systems (Lichtner, 1996) and for some eroding systems (Brantley et al., 2008; Brantley and White, 2009). Several approaches have previously been used to model such complex regolith systems: a graphical approach (White, 2002), a spreadsheet model approach (White et al., 1996, 2008; Boyle, 2007), an analytical approach (Brantley et al., 2008), and reactive transport modeling (Lichtner, 1996; Maher et al., 2009).

The other key feature of a reaction front is the advance rate, ω_m (m y^{-1}), i.e., the rate at which the depth of the midpoint of the reaction front, Z_m^{mid} (m) moves downward with time. We define Z_m^{mid} as the depth where $\tau \approx -0.5$, i.e., the depth where mineral concentration is = 50% of the parent concentration (Fig. 2). The ω_m for a single-component, single-mineral profile is a function of mineral solubility, parent composition, and fluid flow velocity is written as:

$$\omega_m = \frac{v_a(C_{\text{eq}} - C_0)\bar{V}_m}{V_m^o} \quad (5b)$$

where C_{eq} is the aqueous concentration of an element or molecule at chemical equilibrium with a mineral (mol m^{-3}), C_0 is the aqueous concentration of an element or molecule (mol m^{-3}), and \bar{V}_m is the molar volume of mineral m . Note that the kinetic and surface area terms are not in this equation and thus ω_m is independent of kinetics for a single-component, single-mineral profile. For the derivation of this equation, see Lichtner (1988). Although these simple analytical expressions are useful, only with a reactive transport code like FLOTRAN (Lichtner, 2007) can coupled and complex processes be modeled to understand the slopes and advance rates of reaction fronts and how mineral dissolution rates are affected by secondary mineral precipitation, pH change, fluid flow velocity, and the approach to chemical equilibrium.

3.2. Merced parent material mineralogy and surface area

The parent material used as model input in this study is identical to parent material described for other studies of the Merced chronosequence (Table 2; Harden, 1987; White et al., 1996) except that biotite and hornblende were excluded. Biotite does not dissolve but instead transforms to hydrobiotite and then vermiculite as it weathers (White et al., 1996). Approximately 65% of the hornblende is depleted from the soil by 250 ka (White et al., 1996). The relatively low concentrations and rapid depletion of hornblende indicate that feldspar – particularly plagioclase – dissolution dominates soil solution chemistry through much of the chronosequence history. Additionally, the scarcity of thermodynamic and kinetic data for hornblende makes the modeling of this mineral relatively unconstrained. The BET specific surface area (S_m , $\text{m}^2 \text{g}^{-1}$) of a

Table 2
Parameters describing parent material.

Mineral	Merced			Davis Run		
	Specific BET surface area (m ² g ⁻¹) ^a	Volume fraction	Volumetric BET surface area (x10 ⁴ m ² m ⁻³) ^b	Specific BET surface area (m ² g ⁻¹) ^c	Volume fraction	Volumetric BET surface area (x10 ⁴ m ² m ⁻³) ^b
Kaolinite	1.485	0.035	13.65	1.485	0.010	3.861
<i>k</i> -Feldspar	0.372	0.087	8.279	0.210	0.265	13.53
Muscovite	Not measured	Not present		0.550	0.127	18.62
Plagioclase	0.636	0.250	42.10	0.359	0.206	18.57
Quartz	0.274	0.243	17.69	0.155	0.363	14.15
Porosity		0.340			0.070	

^a Calculated from measured specific surface areas from the Merced soils (White et al., 1996) and grain size distribution (Harden, 1987). See Appendix B for more details.

^b See Section 3.3 for details.

^c See Section 3.4 for details.

mineral *m* in the Merced parent material was estimated from measured grain size distributions and roughness factors calculated from mineral-specific BET measurements (Appendix B, White et al., 1996). Roughness is defined here as the mineral surface area measured at one scale (e.g., BET surface area) divided by the same area measured at another scale (e.g., geometric surface area) (Brantley et al., 1999). For the clay fraction, S_m was set to the average measured values of BET surface area for clay fractions from the Post-Modesto and Modesto soils (White et al., 1996) and the clay was modeled as kaolinite (see Section 2.1). The measured volumetric surface area for mineral *m* in the parent material ($A_{B,m}^o$, m² mineral m⁻³ soil) was calculated from S_m :

$$A_{B,m}^o = S_m \rho_m V_m^o \quad (6)$$

where ρ_m is the density of mineral *m* (g m⁻³). In recognition that the reactive volumetric surface area for a mineral *m* ($A_{r,m}^o$, m² mineral m⁻³ soil) may differ from $A_{B,m}^o$, $A_{r,m}^o$ was allowed to vary as the primary fitting parameter for modeling the slope of reaction fronts, which is set by kinetic reactions (Eq. (5a)). Changes in mineral surface area (both $A_{B,m}^o$ and $A_{r,m}^o$) were modeled as:

$$A_m = A_m^o \left(\frac{V_m}{V_m^o} \right)^\gamma \quad (7)$$

Here A_m^o is the volumetric surface area of the mineral in the parent material (m² m⁻³) and γ is the exponent for the relationship between surface area and volume. The exponent γ is usually assumed to be 2/3 based on the relationship between surface and volume for a Euclidean surface (e.g., Brantley et al., 1999).

3.3. Davis Run parent material mineralogy and surface area

Published mineral volume values in the Davis Run parent material (Seiders et al., 1975) did not include porosity and were re-calculated to account for the 7% porosity found in the weathered bedrock (Table 2). The $A_{B,m}^o$ values for plagioclase, *k*-feldspar and quartz at Davis Run were calculated using measured S_m for the sand-size classes from Merced (Table 2). The S_m for muscovite was assumed to

be equal to laboratory-ground muscovite (Knauss and Wolery, 1989). Unlike the Merced parent material, which contains a small fraction of kaolinite, no kaolinite was observed in the Davis Run parent. The kaolinite V_m^o was set to 0.01 in the Davis Run parent material to provide surfaces for kaolinite to precipitate (Table 2). As with Merced, biotite was not included in the model parent material.

3.4. Model specifications

The systems were modeled as one-dimensional columns of homogeneous, porous material that started with parent composition at time 0. Beginning at time 0, an input solution was allowed to infiltrate the column. Models were run until model time equaled soil formation time (Merced) or residence time (Davis Run). The model profile depth was 7.6 m for Merced and 23 m for Davis Run, i.e., the models extended from the land surface to just below the deepest part of the observed reaction fronts.

For both Merced and Davis Run, the thickness of model grid cells ranged from 0.0001 (near the surface) to 0.1 m (at depth). Reaction front depth and slope were observed to be relatively insensitive to maximum model grid sizes ranging from 0.0001 to 0.1 m. Model results were also insensitive to the maximum time step over a range from 1 to 300 y. The model solution algorithm is a hybrid between central finite difference and first order upwinding (Lichtner, 2007). Mineral volume fractions were updated at each node in the column using an explicit finite difference algorithm in time. We assumed concentration-gradient and zero-gradient boundary conditions for the upper and lower boundaries, respectively.

3.4.1. Climate and hydrology

Mesoscale climate modeling predicts MATs at the last glacial maximum (LGM) were at least 5 °C colder than current MATs at both sites, and MAPs at the LGM were higher than present day for northern California and lower for northern Virginia (Bromwich et al., 2004). At a site near Davis Run, paleotemperature data suggest for ≥ 80 ka,

average MATs were more than 5 °C colder than the present (Aeschbach-Hertig et al., 2002). Oxygen isotope measurements of kaolinite also indicated that weathering at Davis Run predominantly occurred during cooler glacial climates (Elliott et al., 1997). Given that most of the weathering in these profiles took place during cooler glacial climates, the Merced model MAT was set to 6 °C, which is 5 °C cooler than current average temperatures in the winter. The winter season is when the overwhelming majority of the precipitation falls and weathering occurs at Merced. The Davis Run model MAT was set to 5 °C.

Detailed discussions of hydrological characteristics at Merced, where hydrologically unsaturated flow dominates, have been published previously (Green et al., 2005; White et al., 2005). These studies demonstrate that a significant control on the hydrology is an argillic horizon that increases in thickness and clay concentration with soil age. This argillic horizon, which begins at 1 m below the surface and evolves with time to as deep as 2 m, serves as a hydrologic “filter.” This filter attenuates the variability that arises from a rainy winter and dry summer. As a result, flow velocities across and below that horizon are approximately constant throughout the year (White et al., 2005).

The model porosity for the Merced parent material was set equal to 0.34, the calculated value for the Riverbank soil (White et al., 2005) from the parent material bulk density of 1.72 g cm⁻³ (Harden, 1987; White et al., 1996). The model porosity for the Davis Run parent material was set equal to 0.07, the value calculated for weathered granite 1 m below the bedrock-saprolite interface based on bulk density measurements (Pavich et al., 1989) and a grain density of 2.7 g cm⁻³. Porosity was updated throughout the simulation as minerals dissolved or precipitated. Merced was modeled under both hydrologically saturated and unsaturated conditions to test sensitivity. In contrast, the lower part of the Davis Run saprolite is saturated or nearly saturated hydrologically and serves as a reservoir for groundwater (Pavich et al., 1989), and thus Davis Run was modeled as a hydrologically saturated system.

For the 250 ka Merced soil, the fluid flow velocity, v (m y⁻¹) equaled 0.057 for the time period of observation from 1990 to 1994 (White et al., 2005). This velocity was calculated from known MAP and measured enrichment of chloride concentrations in soil pore water caused by evapotranspiration (ET) relative to precipitation (White et al., 2005). For Davis Run, a value of v of 0.23 m y⁻¹ was calculated from the water budget including precipitation, evaporation, and runoff (Pavich et al., 1989). Instead of using values of v estimated for one time period of observation of the water budget, we modeled soil development by setting a value for v_a for that location. As discussed below, we first set $v_a = v$ but then allowed v_a to differ from 0.057 or 0.23 m y⁻¹ for the two locations to achieve a best fit.

With the average grain size (sand) and measured flow velocities found at both Merced and Davis Run, data from laboratory studies (Oelkers, 1996) indicate transport by molecular diffusion is more important than transport by longitudinal dispersion. Therefore, dispersion was set to 0 in all models unless otherwise stated. The effective diffusion coefficient, D_e , was calculated using Archie's Law:

$$D_e = D * \phi^2 \quad (8)$$

where D is diffusivity in water (1×10^{-9} m² s⁻¹) and ϕ is porosity (Table 2). Note that 2 is the cementation exponent value for packed sand. Diffusivity was assumed to be species-independent and constant across all grid cells.

3.4.2. Aqueous chemistry and thermodynamic data

Thermodynamic data for primary (or basis) and secondary aqueous species (Table 3) were derived from the EQ3/6 database (Wolery, 1992) with the exception of Al(OH)_{4(aq)}⁻ (Johnson et al., 1992). The model contains the minerals, pore fluid, and CO_{2(g)} as phases. All homogeneous aqueous reactions are assumed to be at equilibrium within each grid cell.

Input solution chemistry for Merced was assumed equal to the average measured precipitation chemistry at the Modesto, Riverbank, and Turlock Lake sites (Table 4, for more details on measured data see White et al., 2005). Input solution chemistry for Davis Run was estimated from the average of the precipitation chemistry for sites MD99, VA00, and VA10 (with sampling periods of 2004–2006, 1984–2006, and 2003–2006, respectively) in the National Atmospheric Deposition Program (Table 4; NADP, 2008). Al and Si concentrations were below the detection limit in Merced precipitation samples and NADP does not report these elements. Thus Al and Si concentrations in the initial precipitation chemistry for both sites were set three orders of magnitude lower than the lowest measured concentrations at Merced (Table 4).

At both sites, water loss via ET reduces the amount of water that infiltrates the profiles and results in an increase in the concentration of ions in the soil solutions as compared to precipitation inputs. At both sites, the ratio of v to MAP was ~0.2, i.e., 80% of precipitation water was lost to ET. Therefore, the model input solutions had concentrations ~5 times higher than precipitation concentrations (Table 4), and these enrichments were calculated using PHREEQC (Parkhurst and Appelo, 1999).

The pH values for model input solutions were calculated by equilibrating the solutions with pCO₂ = 10^{-2.3} atm (Table 4). Additionally, pCO₂ was set at 10^{-2.3} atm at the

Table 3
Chemical species.

Gas species	Primary aqueous species	Secondary aqueous species
CO ₂	Al ³⁺	AlOH ²⁺
	Ca ²⁺	Al(OH) ₂ ⁺
	Cl ⁻	Al(OH) ₃
	H ⁺	Al(OH) ₄ ⁻
	HCO ₃ ⁻	CO ₂
	K ⁺	CO ₃ ²⁻
	Mg ²⁺	HCl
	Na ⁺	H ₃ SiO ₃ ⁻
	SiO _{2(aq)}	H ₂ SiO ₄ ⁻
		KCl
		NaCl
		NaHCO ₃
		NaOH
		OH ⁻

Table 4
Model input solution chemistry and hydrology.

Ion	Average Merced precipitation chemistry ^a ($\mu\text{mol l}^{-1}$)	Evaporated average Merced precipitation chemistry ^b ($\mu\text{mol l}^{-1}$)	Average Davis Run precipitation chemistry ^c ($\mu\text{mol l}^{-1}$)	Evaporated average Davis Run precipitation chemistry ^b ($\mu\text{mol l}^{-1}$)
Al ³⁺	4.08×10^{-5d}	2.08×10^{-4}	1.04×10^{-6d}	2.08×10^{-4}
Ca ²⁺	20.8	106	1.75	8.92
HCO ₃ ⁻	20.0	pCO ₂ -controlled	12.0	pCO ₂ -controlled
K ⁺	13.8	70.3	0.52	2.65
Mg ²⁺	15.0	76.4	0.71	9.62 ^e
Na ⁺	38.9	198	4.24	21.6
pH	7.00	5.79	7.0	5.79
SiO _{2(aq)}	2.20 ^d	1.12	2.20 ^d	1.12
log pCO ₂ (atm)	-2.3	-2.3	-2.3	-2.3
<i>v</i> (m y ⁻¹)		0.057		0.23
<i>D_e</i> (m ² s ⁻¹)		1.16×10^{-10f}		6.76×10^{-11f}

^a Combination of wet and dry deposition measured for sites where pore water chemistry samples were collected (White et al., 2005).

^b Concentrated with PHREEQC and the LLNL database (Parkhurst and Appelo, 1999) to simulate the effects of evaporation. See text.

^c Average wet deposition chemistry from National Atmospheric Deposition Program sites VA10, MD99, VA00, & PA47 using all data available (3–23 years) for each site through January 2008 (NADP, 2008).

^d Set at three orders of magnitude smaller than lowest concentration measured in Merced pore waters. At one order of magnitude smaller than the lowest measured concentration, the input solution is saturated with respect to quartz (SI = 0.49).

^e Calculated as $3.62 \mu\text{mol l}^{-1}$ but increased in concentration so that the chemistry of the input fluid was charge balanced.

^f Porosities used to calculate $D_e = 0.34$ (value measured for parent material) and 0.20 (calculated value for midpoint of plagioclase reaction front).

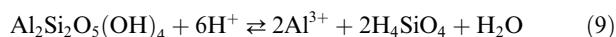
upper boundary of the model. The pCO₂ of $10^{-2.3}$ atm is consistent with the low end of soil pCO₂ values observed for modern temperate ecosystems (Cerling, 1999). While this pCO₂ is slightly lower than the average maximum pCO₂ measured for the 250 ka Merced soil (-2.2, Table EA-5; White et al., 2005), a lower concentration is justified since much of the weathering in these soils occurred during glacial periods when atmospheric CO₂ was lower than the present because of decreased atmospheric CO₂ and lower plant productivity (Bender, 2003).

3.4.3. Mineral thermodynamics and kinetics

All minerals were modeled as pure phases using thermodynamic data from the EQ3/6 database (Wolery, 1992) for primary minerals and from experimental data for kaolinite (thermodynamic and kinetic data summarized in Table 5). The solubilities of Merced plagioclase (An₃₂, White et al., 1996) and Davis Run plagioclase (An₆, Seiders et al., 1975) were modeled as albite. For Merced, when the actual plagioclase (An₃₂) composition was assumed in the model using an ideal mixing relationship to calculate solubility (Lichtner and Carey, 2006), *v_a* had to be reduced by several orders of magnitude compared to *v* to simulate the observed mineral profiles. These models run with An₃₂ also failed to reproduce the observed *k*-feldspar profiles. A similar conclusion was reached in the only comparable published modeling study (Maher et al., 2009). They discussed detailed petrographic studies of An₂₅ to An₈₀ plagioclase in plutonic rocks that demonstrated that the crystals are constructed of submicron-scale, intergrown lamellae of albitic and anorthic compositions (see citations and summary in White et al., 2009). Maher et al. (2009) concluded that anorthic portions of the plagioclase were

shielded from reaction with soil pore waters due to the extremely small nature of the intergrown lamellae and thus assumed albite solubility controlled plagioclase dissolution. The same assumption was made here.

Secondary mineral precipitation in all profiles was modeled as kaolinite precipitation since kaolinite is the dominant secondary mineral in both systems. The kaolinite dissolution-precipitation reaction can be written as:



Several experimental values (May et al., 1986; Nagy et al., 1991; Yang and Steefel, 2008) for the equilibrium constant, *K*, for this reaction ($10^{7.45}$, $10^{7.89}$, $10^{7.30}$) are higher than the similar *K* value at 25 °C in the EQ3/6 database ($10^{6.80}$). Thus, log *K* values for Eq. (9) in the thermodynamic database were increased by 1 relative to the EQ3/6 database (Table 5). Note that here, *K*, is the equilibrium constant for the reaction written as dissolution.

In FLOTTRAN, mineral–water reactions are written as:



where *M_{aq}* is the aqueous species and *M_s* is the reacting mineral. Note the reaction is written where precipitation is the forward reaction, rather than dissolution (Lichtner, 1996). The net rate of dissolution and precipitation for mineral *m*, *R_m* (mol m⁻³ porous material s⁻¹) in FLOTTRAN is written as:

$$R_m = -\text{sgn}_m A_m \left(\sum_l P_l k_l \right) \left| 1 - (K_m Q_m)^{1/\sigma_m} \right|^{\beta_m} \quad (11)$$

In this equation, *P_m* is the prefactor for each parallel reaction defining the product of contributions from primary and secondary aqueous species, *k_m* is the dissolution rate

Table 5
Mineral kinetic and thermodynamic data.

Mineral	Log K at 25 °C ^a	Log k_m (mol m ⁻² s ⁻¹)	Rate law dependence	Reaction order	Activation energy ^b (kJ mol ⁻¹)
Albite far-from-equilibrium	2.7645	-9.62 ^c	H ⁺	0.403 ^c	65.0
		-14.90 ^c	OH ⁻	0.376 ^c	71.0
Albite – Near-equilibrium		-10.84 ^d	H ⁺	0.403 ^c	65.0
		-16.12 ^d	OH ⁻	0.376 ^c	71.0
Kaolinite	7.8101	-14.15 ^e	H ⁺	0.151 ^e	65.9
		-23.79 ^e	OH ⁻	0.894 ^e	17.9
Potassium feldspar	-0.2753	-10.06 ^b	H ⁺	0.50 ^b	51.7
		-12.41 ^b	H ₂ O		38.0
		-21.20 ^b	OH ⁻	0.82 ^b	94.0
Muscovite	13.5858	-11.85 ^b	H ⁺	0.37 ^b	22.0
		-13.55 ^b	H ₂ O		22.0
		-14.55 ^b	OH ⁻	0.22 ^b	22.0
Quartz	-3.9993	-11.36 ^c	H ⁺	0.309 ^c	87.7
		-14.35 ^c	OH ⁻	0.411 ^c	87.7

^a From the EQ3/6 database with the exception of kaolinite (see Section 3.4.3) for dissolution reactions at 25 °C. FLOTRAN recalculates the equilibrium constant at the model temperature.

^b Values from Palandri and Kharaka (2004).

^c Regression of compiled experimental data for far-from-equilibrium dissolution data (Bandstra and Brantley, 2008; Bandstra et al., 2008).

^d Calculated using the relationship between far-from-equilibrium and near-equilibrium dissolution rates observed by Hellmann and Tisserand (2006). See Section 3.4.4 and Fig. 3 for details.

^e One order of magnitude slower than dissolution rate constants (see Section 3.4.3) determined by fit of compiled experimental data for dissolution experiments (Moore, 2008); experimental data from (Carroll-Webb and Walther, 1988; Bauer and Berger, 1998; Huertas et al., 1999; Cama et al., 2002).

constant (mol m⁻² s⁻¹) for each parallel rate law for mineral m , Q_m is the ion activity product and K_m is the equilibrium constant for the reaction written as precipitation (Lichtner, 1988, 1996, 1998). Although the reactions in FLOTRAN are formalized with precipitation as the forward reaction (e.g., Eq. (10)), the rate constant k_m is a dissolution rate constant.

The sign of the rate equation is calculated as:

$$\text{sgn}_m = \frac{1 - (K_m Q_m)^{1/\sigma_m}}{|1 - (K_m Q_m)^{1/\sigma_m}|} \quad (12)$$

A negative rate connotes dissolution and a positive rate connotes precipitation.

To correct rates for chemical affinity, Temkin's constant, σ_m , and the affinity power, β_m , are included (for more details see Lichtner, 2007). Note that when $\sigma_m = \beta_m = 1$, the rate equation is consistent with a transition-state theory (TST) rate law treatment describing one elementary reaction that controls dissolution/precipitation (Brantley, 2008). We therefore call this the TST rate law. Where more than one reaction controls dissolution/precipitation over the full range of chemical affinity, then such a simple TST rate law cannot fully describe the rate behavior. In that case, it is necessary to set these parameters to differ significantly from unity. The supersaturation threshold that must be exceeded for primary minerals to precipitate was set to an arbitrarily high number (10^{99}) since precipitation of these minerals is not expected to occur under earth surface conditions.

The prefactor for each parallel reaction is defined as:

$$P_m = \left[\prod_{p=1}^{N_c} \frac{a_p^{\alpha_p}}{1 + K_p a_p^{\eta_p}} \right] \left[\prod_{s=1}^{N_{ex}} \frac{a_s^{\alpha_s}}{1 + K_s a_s^{\eta_s}} \right] \quad (13)$$

where a_p and a_s represent the activity of primary and secondary aqueous species, K_p and K_s are the equilibrium constants for reactions describing reactions with the primary and secondary species, and α_p , η_p , α_s , η_s are constants. The prefactor is used to formulate rate laws dependent on aqueous species such as H⁺, OH⁻, and Al³⁺.

The rates due to aqueous species such as H⁺ and OH⁻ are modeled as parallel rate laws that are summed to calculate the net rate:

$$R_m = R_m^{\text{H}^+} + R_m^{\text{H}_2\text{O}} + R_m^{\text{OH}^-} \quad (14)$$

where $R_m^{\text{H}^+}$, $R_m^{\text{H}_2\text{O}}$, $R_m^{\text{OH}^-}$ are the rate laws for acidic, water, or basic dissolution, respectively. These rate laws are calculated by using appropriate k_m values for acidic, water, or basic dissolution in Eq. (11). Reaction orders for H⁺ and OH⁻ rates are then used as appropriate in Eq. (13). Rate constants and reaction orders for albite, muscovite, k -feldspar, and quartz are derived from best-fit equations of compiled laboratory results (Table 5). The reaction orders with respect to H⁺ or OH⁻ for kaolinite were calculated based on kaolinite dissolution data. Furthermore, the rate constant for kaolinite, k_{kaol} , was set to be one order of magnitude slower than the laboratory value for dissolution (Table 5) because measured kaolinite precipitation rates are ~ 1 order of magnitude smaller than predicted when

fitting a TST rate law to kaolinite dissolution data (Yang and Steefel, 2008).

FLOTTRAN calculates the rate in each model cell from Eq. (11) using the following inputs: the values of k_m for each rate in Eq. (14) and the reaction order (Table 5) along with the calculated solution chemistry for that cell and the temperature. Activation energies are used in FLOTTRAN to correct rate constants to field temperatures (Table 5). Values for K_m at field temperatures are interpolated between the database values at 0, 25, 60, 100, 150, 200, 250, and 300 using a Mayer–Kelly function (Lichtner, 2007).

3.4.4. Alternative rate laws

In TST-like laws, both dissolution and precipitation rates slow linearly as thermodynamic equilibrium is approached without showing an inflection point because only one elementary reaction controls the rate (Fig. 3). Experimental studies demonstrate that TST-like rate laws for plagioclase overpredict dissolution rates near equilibrium (Burch et al., 1993; Gautier et al., 1994; Oelkers et al., 1994; Taylor et al., 2000; Hellmann and Tisserand, 2006), most likely because more than one rate-limiting step is important across the full range of saturation state (Shiraki and Brantley, 1995; Beig and Lutge, 2006). Instead, near-equilibrium plagioclase dissolution rates are smaller than far-from-equilibrium rates and the net rates of dissolution change sigmoidally as a function of ΔG of reaction as

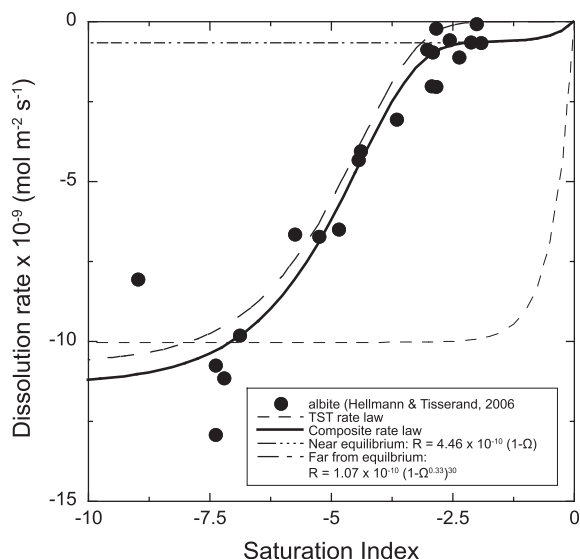


Fig. 3. Laboratory rate data (circles) and fitted composite rate law for far-from-equilibrium and near-equilibrium conditions at 150 °C. Plagioclase dissolution rates (circles) versus saturation index (Ω) data from Hellmann and Tisserand (2006). Dissolution rates decrease in a sigmoidal fashion as the saturation index increases. These rates are used to calculate a composite dissolution rate law (solid line) from the summation of far-from-equilibrium (dashed [long] line) and near-equilibrium (dashed-dotted line) rate equations. This formulation does not contain the mechanistic data from the parallel rate laws used by Hellmann and Tisserand (2006) to fit the data but this composite rate law is mathematically equivalent in following the approach of Maher et al. (2006). A TST rate law (dashed [short] line) is also included on the plot for comparison.

chemical equilibrium is approached (Burch et al., 1993; Brantley, 2004; Hellmann and Tisserand, 2006). To formulate an appropriate rate law that describes the sigmoidal rate behavior, albite dissolution data collected at 150 °C and pH 9.2 and across a range of equilibrium conditions (Hellmann and Tisserand, 2006) were empirically fit with two rate laws (Fig. 3) following (Maher et al., 2006). The Temkin's coefficient and chemical affinity power for the near-equilibrium and far-from-equilibrium rates were assumed to be constant with temperature but k_m was allowed to vary according to the Arrhenius equation (activation energies in Table 5). The empirical fit of the rate data (Fig. 3 and Table 5) yields the following rate equation for proton-promoted dissolution for plagioclase:

$$R_m^{H^+} = k_m^{FFE} A_m [1 - (Q_m K_m)^{1/3}]^{30} + k_m^{NE} A_m [1 - (Q_m K_m)] \quad (15)$$

where k_m^{FFE} is the dissolution rate constant for the mechanism that dominates far from equilibrium and k_m^{NE} is the rate constant for the mechanism that dominates near equilibrium.

Several researchers have reported that, in addition to sigmoidal rate behavior, aqueous Al^{3+} cations inhibit plagioclase (and other aluminosilicate) dissolution even under far-from-equilibrium conditions (e.g., Gautier et al., 1994; Oelkers et al., 1994). The following equation has been proposed (Oelkers et al., 1994) for inhibition of alkali feldspar dissolution at far from equilibrium conditions:

$$R_m = k_m A_m \left(\frac{\frac{a_{H^+}^{3h}}{a_{Al^{3+}}^h} \prod_i a_i^{v_i}}{1 + K \cdot \frac{a_{H^+}^{3h}}{a_{Al^{3+}}^h} \prod_i a_i^{v_i}} \right) \quad (16)$$

where m = plagioclase. The coefficient h is 0.33 and K is the equilibrium constant for the formation of the silica-rich precursor to dissolution on the mineral surface. When the denominator approaches one and when no other precursor species are involved, only the numerator of the precursor term is necessary. Thus, the following equation was used to model aluminum-inhibition:

$$R_m = k_m A_m \left(\frac{a_{H^+}^{3h}}{a_{Al^{3+}}^h} \right) (1 - (K_m Q_m)^{1/3}) \quad (17)$$

With the pH and Al concentration values for Merced (pH 6–8, dissolved Al^{3+} concentration 1×10^{-9} to 1×10^{-13} M, see White et al., 2005), the largest possible difference in rate between the full (Eq. (16)) and simplified (Eq. (17)) versions of the Al-inhibition rate law is always observed to be <10%.

4. RESULTS

A baseline model was run to simulate the Merced 250 ka profile and then a series of sensitivity tests were performed to understand which parameters control the weathering advance rate, ω_m , which in turn controls Z_m^{mid} , and the reaction front thickness, L_m . In addition, a series of best-fit models were developed and then compared to field data for both Merced and Davis Run.

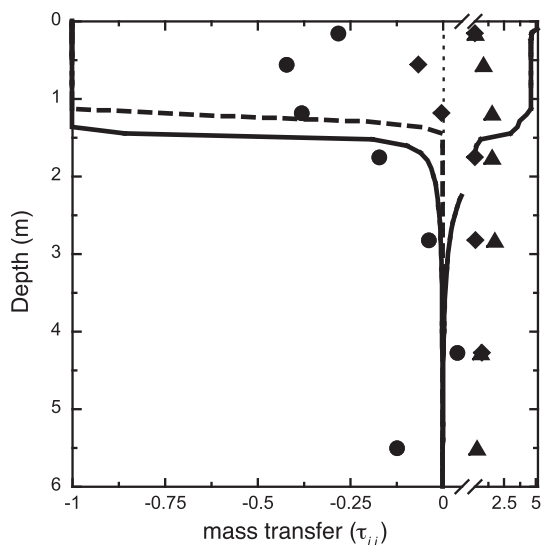


Fig. 4. Baseline model in comparison to 250 ka Merced profile data. Depth versus $\tau_{j,q}$ for model reaction fronts for j = plagioclase (solid line), k -feldspar (dashed line), and $\tau_{j,q}$ for kaolinite (solid line, $\tau_{j,q}$) versus field reaction fronts for plagioclase (circles), k -feldspar (diamonds), and kaolinite (triangles).

4.1. Merced baseline model

Baseline models were run with laboratory-measured values for k_m (Table 5), TST-like rate laws ($\sigma_m = \beta_m = 1$, see Eq. (11)), $A_{r,m}^o$ equals the measured values ($A_{B,m}^o$, Table 2), and v_a set equal to v (Table 4). To start with, hydrological saturation, H , was assumed to equal 100% in the baseline model runs.

After 250 ka, the model-predicted Z_{plag}^{mid} was deeper than observed and L_{plag} was much steeper than observed (Fig. 4). Predicted F_{plag} equaled 70.2% compared to the observed 86.6% (over the upper 5 m). At 600 ka (not shown), model-predicted F_{plag} equaled 18.0% and was much smaller than the observed F_{plag} of 77.4% (over the upper 4.25 m). The model predicted significant k -feldspar dissolution at 250 ka (Fig. 4) and 600 ka (not shown), whereas no k -feldspar dissolution was observed in those soils (Table EA-3). In contrast, the predicted F_q (not shown) in the baseline model was close to the observed and equaled $\sim 89.0\%$ after 3000 ka (over the upper 5 m). Modeled quartz dissolution was confined to the upper 0.6 m. At 250 ka, kaolinite concentrations are overpredicted from 0 to 1.5 m and underpredicted from 1.5 to 6 m (Fig. 4).

4.2. Merced baseline model sensitivity

Baseline model sensitivity to variations in several parameters was explored to determine key parameters controlling Z_m^{mid} and L_m , particularly for plagioclase. The following parameters were varied relative to the baseline model and compared to the 250 ka profile: temperature (± 5 °C), diffusion coefficient, D (1×10^{-5} and 1.16×10^{-6} cm² s⁻¹), dispersivity (0.01–0.1 m, physically reasonable values for the Merced system), and the surface area exponent, γ (0.01–1). Predicted Z_{plag}^{mid} and L_{plag} varied $< 5\%$ for models run with

parameters within these ranges. Additionally, the baseline model was run with the sigmoidal or aluminum-inhibition rate laws previously described with minimal difference in the predicted model results. Results for parameters that affect model predictions significantly are delineated below.

Model-predicted Z_{plag}^{mid} and Z_{plag}^b significantly changed with variations in H (Fig. 5A), k_{kaol} (Fig. 5A), v_a (Fig. 5B), or pCO₂ at the upper boundary (Fig. 5C). Reducing H from 100% to $< 100\%$ had the largest effect on the baseline Z_{plag}^{mid} (Fig. 5A). Once H was $< 100\%$, the exact value was not significant at the relatively low flow velocities relevant for the Merced profiles. When H was $< 100\%$, the predicted Z_{plag}^{mid} was several meters deeper than the observed (Fig. 6A). Predicted pH was higher and plagioclase was closer to equilibrium in models run with $H = 100\%$ than predicted values when H was $< 100\%$ (Fig. 6B and C). Plagioclase dissolution and kaolinite precipitation rates were slower in the model where $H = 100\%$ (Fig. 6D).

When $H < 100\%$, to predict Z_{plag}^{mid} values that match the field, we had to set a value for advection, v_a , that was much smaller than v , a value of k_{kaol} much lower than measured in the laboratory (Table 5), or some combination of the two. Changing only v_a required an order of magnitude decrease relative to v (0.057 m y⁻¹ to 0.0057 m y⁻¹). This large decrease in v_a is unlikely, particularly since an estimated value for transport by diffusion in this soil was 0.0073 m y⁻¹. When k_{kaol} were set equal to laboratory values (Table 5) and H was $< 100\%$, predicted Z_{plag}^{mid} (Fig. 5A) and Z_{kf}^{mid} (not shown) were much deeper than the observed. In comparison, reducing k_{kaol} by two or four orders of magnitude resulted in a predicted Z_{plag}^{mid} that was approximately 1.25 and 0.25 m deeper than observed, respectively (Fig. 5A). When kaolinite is not allowed to react, the predicted Z_{plag}^{mid} is shallower than the observed (Fig. 5A) due to the model solution rapidly approaching equilibrium with respect to plagioclase. Although the predicted Z_{plag}^{mid} best matched the field for 250 ka (Fig. 5A) and 600 ka (not shown) when k_{kaol} was reduced by four orders of magnitude and $v_a = v$, k -feldspar dissolution for the 3000 ka soil was significantly underpredicted and the kaolinite saturation index (SI) prediction for the 250 ka soil was 4–5, which was higher than observed (White et al., 2005). Setting k_{kaol} two orders of magnitude smaller than the experimental value when H was $< 100\%$ resulted in a predicted kaolinite SI of 1–2 (Fig. 6C), which is the same range observed in the soil pore waters (White et al., 2005). Thus adjustments to both v_a and k_{kaol} better matched the system than large adjustments to solely v_a or k_{kaol} .

With H set to $< 100\%$ and k_{kaol} set two orders of magnitude smaller than experimental values (Table 5), the sensitivity of Z_{plag}^{mid} was tested by varying v_a , pCO₂ at the upper boundary, and temperature. Changes in v_a have the largest effect on the baseline model-calculated Z_{plag}^{mid} : a 50% decrease or increase resulted in a $\sim 50\%$ shallower or deeper Z_{plag}^{mid} and Z_{plag}^b , respectively (Fig. 5B). Shifting pCO₂ values at the upper boundary had a much smaller effect: pCO₂ = $10^{-2.1}$ atm resulted in Z_{plag}^{mid} and Z_{plag}^b shifting $\sim 13\%$ deeper than baseline while pCO₂ = $10^{-2.5}$ atm resulted in Z_{plag}^{mid} and Z_{plag}^b shifting $\sim 12\%$ shallower (Fig. 5C). A 5 °C temperature change (not shown) resulted

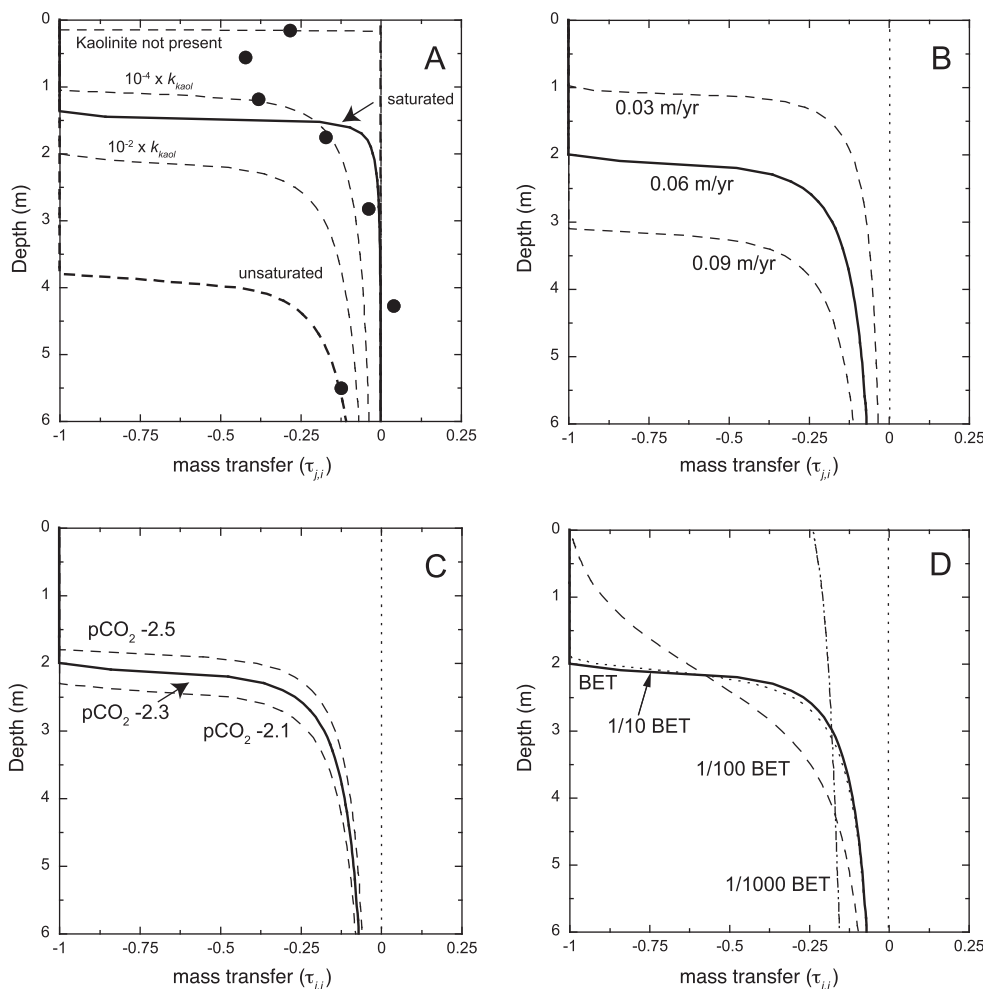


Fig. 5. Model sensitivity tests to determine controls on reaction front depth and slope with reference to Merced 250 ka profile. Depth versus $\tau_{plag,q}$ for field data (circles) and baseline models run with a range of input parameters to test sensitivity at 250 ka. Parameters that were varied include: (A) saturated (solid line) versus unsaturated flow (dashed lines) and a range of kaolinite rate constants, (B) flow velocity, (C) log pCO_2 , and (D) reactive surface area. In (D), the dark line represents a model where k_{kaol} values are 10^{-2} slower than the values in Table 5. Variations in clay kinetics, flow velocity, and pCO_2 primarily affect the depth of the plagioclase reaction front. Only changes to the reactive surface area (or product of the rate constant and surface area) affect the weathering gradient. Note in (D) that decreases in A_{plag}^o cause steeper slopes but that the inflection point of the reaction front remains the same until the value of A_{plag}^o is so low that the profile becomes incompletely developed and the reaction front becomes almost vertical.

in similar changes to predicted Z_{plag}^{mid} as those predicted for the pCO_2 variations described above. While changes in k_{kaol} , v_a , pCO_2 , or temperature affected Z_{plag}^{mid} and Z_{kf}^{mid} , none of these parameters significantly affected L_{plag} and L_{kf} (Fig. 5A–C).

Given these observations, it is clear that model flow velocity is constrained both by v based on the current water balance and by observations of Z_{plag}^{mid} and Z_{kf}^{mid} . Given those two constraints on the velocity, the only way to significantly change the modeled L_{plag} is to change the value of $k_{plag}A_{plag}^o$ (Eq. (11), Fig. 5D). Little is known about reactive surface area. In contrast, a large body of data has been compiled for laboratory rate constants (e.g., Brantley, 2008); therefore, we assume that k_{plag} is equal to the laboratory value. We therefore tune $A_{r,m}^o$ to achieve model profiles that match the observed. Reducing $A_{r,m}^o$ by two to three orders of

magnitude relative to $A_{B,plag}^o$ is necessary to predict model L_{plag} similar to the observed (Fig. 5D).

4.3. Merced best-fit models

As shown in the previous section, Merced was modeled successfully with the following approach. First, the value for H was established. Second, k_{kaol} was set to a value that resulted in accurate prediction of measured k -feldspar dissolution and kaolinite SI values. Third, the observed value of Z_{plag}^{mid} (the most soluble mineral) was used to constrain the best-fit value for v_a . Once a value for v_a was determined, the model-predicted values of L_m were matched to field data by tuning $A_{r,m}^o$ for each mineral.

The primary criterion used for the best-fit models was minimization of the sum of the square of the errors between

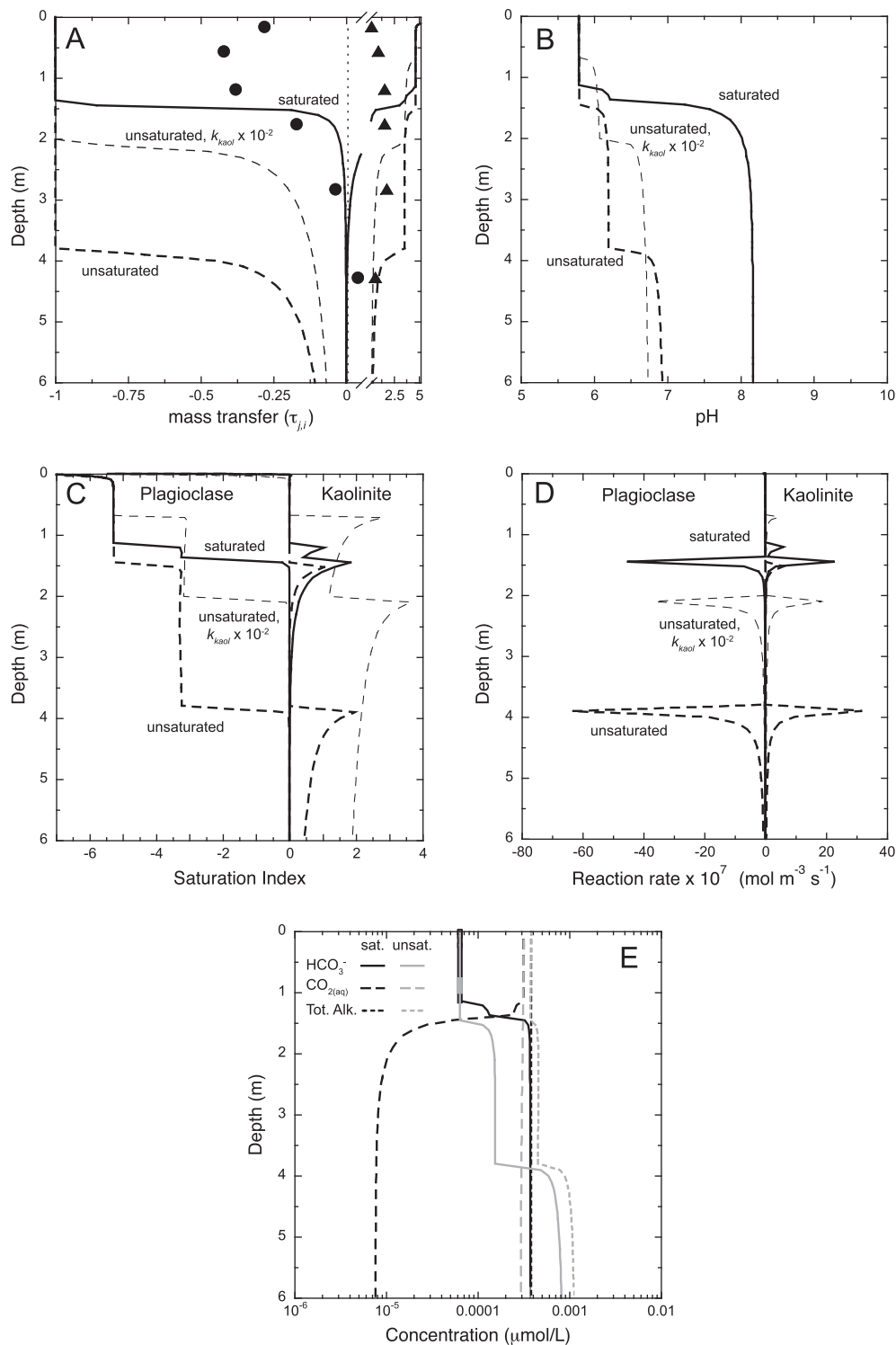


Fig. 6. Comparison of model runs with laboratory k_{kaol} and hydrologically saturated (thick solid line), laboratory k_{kaol} and hydrologically unsaturated (thick dashed line), or $k_{kaol} \times 10^{-2}$ and hydrologically unsaturated (thin dashed line). Depth versus (A) $\tau_{j,q}$ for model reaction fronts for j = plagioclase and kaolinite (solid lines) versus 250 ka field data for plagioclase (circles) and kaolinite (triangles), (B) pH, (C) saturation indices for plagioclase and kaolinite, (D) plagioclase and kaolinite reaction rates plotted per m³ of porous medium for models run with the kaolinite rate constants set at values given in Table 5 (solid lines) or 10^{-2} smaller than the values in Table 5 (dashed lines), and (E) carbon species for saturated versus unsaturated models. The upper step in the (B) pH, (C) SI, and (D) rate curves represents the k -feldspar reaction front and the lower step represents the plagioclase reaction front. In (E), total alkalinity in the saturated model remains constant at $\sim 4 \times 10^{-4}$ $\mu\text{mol/L}$ and CO_{2(aq)} in the unsaturated model remains nearly constant.

Table 6
Best-fit models.

Model best-fit flow velocity (m y ⁻¹)	Adjustment factor ($A_{B,m}^o/A_{r,m}^o$)			Observed volume remaining (F_j)	Modeled volume remaining (F_j)
	For best-fit with TST rate laws	For best-fit with Al-inhibition rate law	For best-fit with sigmoidal rate law		
Merced					
<i>40 and 250 ka</i>					
<i>k</i> -Feldspar	250				99.2
Plagioclase	0.016	468	49.5	46.8	86.7
Quartz		240			100
Kaolinite					120
<i>600 ka</i>					
<i>k</i> -Feldspar		556			98.9
Plagioclase	0.009	936	117	93.6	77.4
Quartz		540			100
Kaolinite					170
<i>3000 ka</i>					
<i>k</i> -Feldspar		974			19.5
Plagioclase	0.13	1560	105	468	4.97
Quartz		983			99.3
Kaolinite					460
Davis Run					
Muscovite		211			
<i>k</i> -Feldspar	0.17	194			
Plagioclase		53.0	5.3	6.2	27.0
Quartz		40.1			27.0

the model-predicted and field values of L_{plag} (250, 600, 3000 ka soils) and L_{kf} (3000 ka soil). We also used a secondary criterion: model and field F_m for plagioclase and *k*-feldspar were constrained to be <3% different for each mineral. The field observations for the 40 ka soil rely on only two depth values. Therefore, the best-fit parameters for the 40 ka soil were assumed to be the same as the 250 ka soil. Because significant *k*-feldspar dissolution is only observed for the 3000 ka soil and no quartz dissolution was observed through 3000 ka, the values for $A_{r,m}^o$ for *k*-feldspar and quartz were first tuned to match *k*-feldspar and quartz profiles at 3000 ka. For models predicting dissolution for soils of age $y < 3000$ ka, the *k*-feldspar and quartz values for $A_{r,m}^o$ were calculated as:

$$\frac{\left(\frac{A_{r,m}^o}{A_{B,m}^o}\right)_y}{\left(\frac{A_{r,m}^o}{A_{B,m}^o}\right)_{3000}} = \frac{\left(\frac{A_{r,plag}^o}{A_{B,plag}^o}\right)_y}{\left(\frac{A_{r,plag}^o}{A_{B,plag}^o}\right)_{3000}} \quad (18)$$

In other words, the ratio of $A_{r,m}^o$ to $A_{B,m}^o$ for *k*-feldspar and quartz between each younger soil ($y = 250$ and 600 ka) and the 3000 ka soil was set to approximately the same ratio as $A_{r,m}^o$ to $A_{B,m}^o$ for plagioclase between each younger soil and the 3000 ka soil.

Best-fit predictions for Z_{plag}^{mid} require that v be multiplied by ~ 0.3 , 0.2, and 2.3 for the 250, 600, and 3000 ka soils, respectively, to calculate v_a (Table 6). To match model and field values of L_{plag} for the 250, 600, and 3000 ka soils (Figs. 7A and 8), $A_{r,plag}^o$ was decreased relative to $A_{B,plag}^o$ by factors of 470, 940, and 1600, respectively (Table 6). Predicted saturation indices and reaction rates for the 250 ka profile also are shown (Fig. 7B and C).

Plots of best-fit models for each profile also show predicted plagioclase reaction fronts for each of the other Merced soils (Figs. 7A and 8). For the 250 and 600 ka soils, modeled *k*-feldspar and quartz dissolution are minimal. At 3000 ka, v_a values were set so as to accurately predict the *k*-feldspar front. Model kaolinite concentrations in all profiles are highest at the surface and decrease with depth (Figs. 7A and 8). The average model and field kaolinite enrichment over the top 5 m (or top 4.25 m for 600 ka) are similar: predicted values for $\tau_{kaol,q}$ of 1.6, 1.7, and 5.2 as compared to observed values of 1.2, 1.8, and 5.6 for the 250, 600, and 3000 ka soils, respectively. Predicted clay concentrations are higher than observed in the upper meter and lower than observed for intervals deeper than 1.5 meters (Figs. 7A and 8).

4.4. Solution chemistry predictions

An additional constraint on these models not used thus far is the measured pore fluid chemistry. The best-fit Merced model described in the previous section for the 250 ka soil also predicted the pore water chemistry well for that same soil (Fig. 9; for more details on pore water chemistry see White et al., 2005). Predicted pH values were similar to pH values calculated for each depth interval by using average measured soil pCO₂ and alkalinity as inputs for PHREEQC (Fig. 9A). It was necessary to calculate pH values for the field samples because pH values as originally measured were high due to the degassing of CO₂ from solutions within the suction lysimeters (White et al., 2005). Model-predicted alkalinity and Na concentrations also matched the

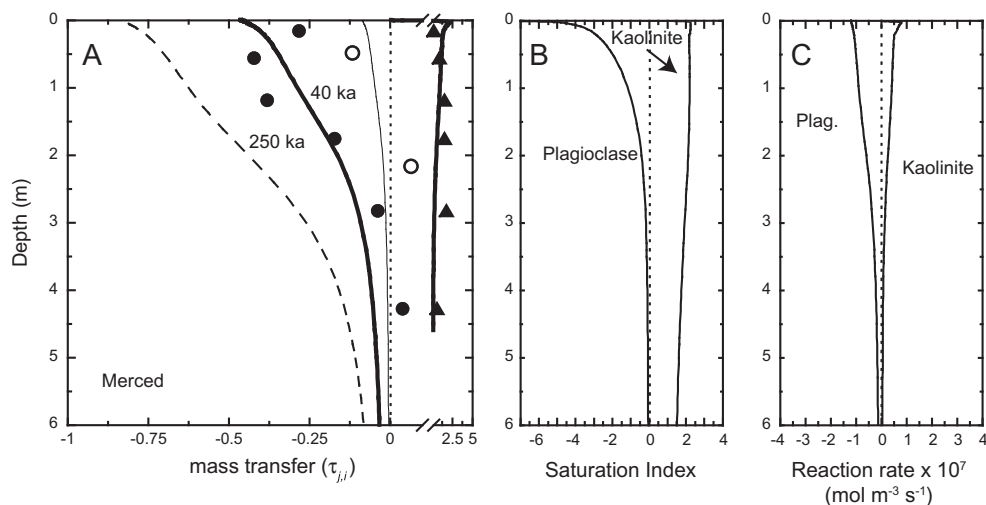


Fig. 7. Best-fit model for Merced 250 ka profile. Profiles are shown for (A) $\tau_{j,i}$ for model reaction fronts for plagioclase (at 40 ka: thin solid line, 250 ka: thick solid line, 600 ka: dashed line, 3000 ka front is >6 m depth) and $\tau_{j,q}$ for kaolinite (solid line) versus field reaction fronts for plagioclase (40 ka open circles, 250 ka filled circles) and kaolinite (250 ka triangles), (B) Profiles showing saturation indices calculated for plagioclase and kaolinite. (C) Profiles showing calculated plagioclase and kaolinite reaction rates per m^3 of porous medium. Best-fit model was run for hydrologically unsaturated conditions as described in text.

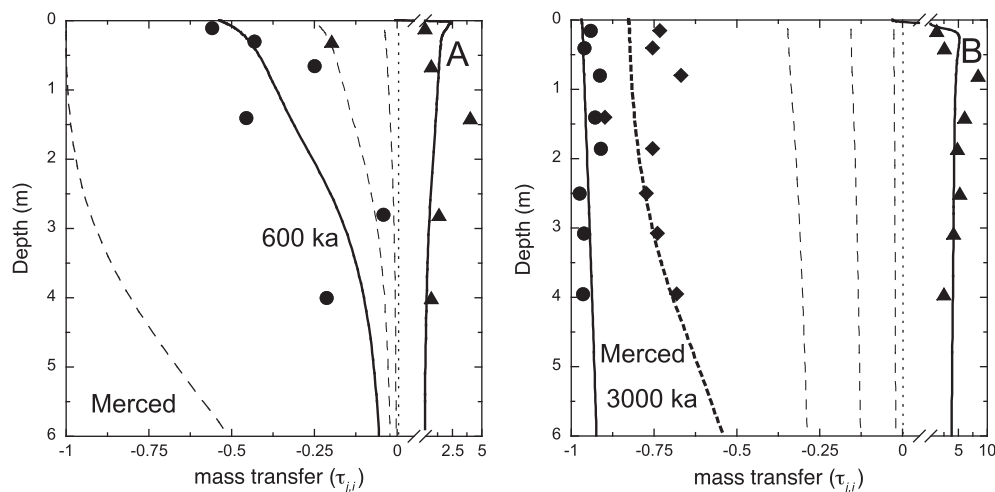


Fig. 8. Best-fit models for Merced (A) 600 ka and (B) 3000 ka profiles. (A) Profiles of the $\tau_{j,i}$ for model reaction fronts for plagioclase (600 ka: thick solid line, 40, 250, and 3000 ka: thin dashed lines). $\tau_{kaol,q}$ values are shown as solid line for model output and triangles for observations. (B) $\tau_{j,i}$ model reaction fronts for plagioclase (3000 ka: thick solid line, 40, 250, and 3000 ka; thin dashed lines) and k -feldspar (thick dashed line) and $\tau_{kaol,q}$ (solid line). Observed concentrations are shown as symbols for plagioclase (circles), k -feldspar (diamonds) and kaolinite (triangles). Dotted lines in all figures indicate where the mass transfer coefficient = 0.

observed (Fig. 9B and C). The model-predicted concentrations for SiO_2 were somewhat lower than measured, particularly in the upper two meters (Fig. 9D). Model pore water Al concentrations decreased from 11.6×10^{-4} to $5.43 \times 10^{-4} \mu\text{mol L}^{-1}$ over 2.5–5.0 m depth compared with measured mean Al concentrations of 593×10^{-4} , 1.4×10^{-4} , and $1.0 \times 10^{-4} \mu\text{mol L}^{-1}$ at 2.59, 3.05, and 3.66 m depths, respectively (not shown). Measured Al concentrations included all Al species, including Al-organic complexes (White et al., 2005). Model Al concentrations were lower than the observed for the upper 3 m. The higher observed Al concentrations were likely due to Al-organic

complexes with free Al concentrations significantly lower than total Al concentrations (Lundström et al., 2000; Masiello et al., 2004; White et al., 2005).

Some of the discrepancies between modeled and measured pore water chemistry were likely due to the fact that the model tuned to fit the mineralogy profiles was constrained with $p\text{CO}_2$ and temperature values lower than measured currently. We tested the effects of using current values for $p\text{CO}_2$ ($\log p\text{CO}_2 = -2.1$ for the 250 ka soil, White et al., 2005) and average winter temperature (11°C) in a second set of models. The second set of models used the output values for A_m and V_m for each mineral

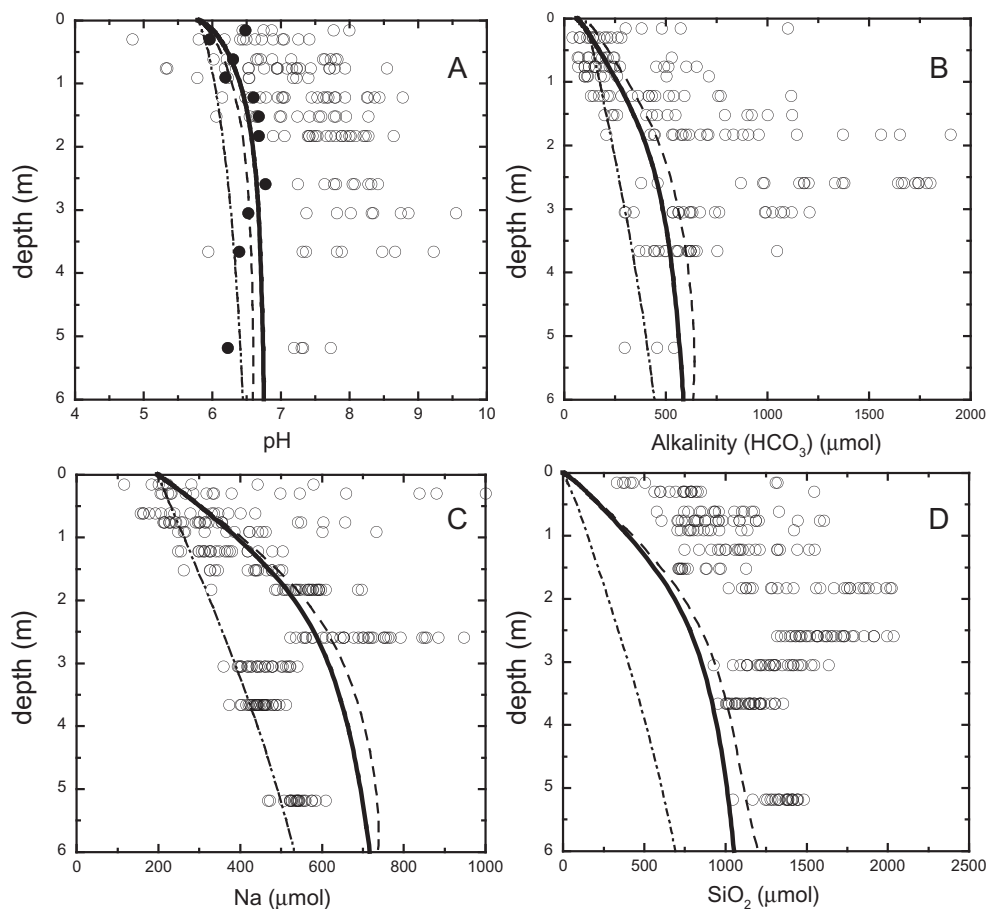


Fig. 9. Best-fit model results for Merced 250 ka pore fluid chemistry. The best-fit models were determined strictly on the basis of solid-phase chemistry as discussed in the text. Calculated porewater chemistry for those models are shown here. Profiles of model-predicted (A) pH, (B) alkalinity, (C) Na, and (D) SiO_2 concentrations are shown as a solid line, see also Fig. 6). A second model prediction is shown for models run and maintained in equilibrium with measured modern 250 ka soil pCO_2 ($\log \text{pCO}_2 = -2.1$), the average winter temperature 11°C , with the same flow velocity (0.016 m y^{-1}) as the best-fit mineralogy model (dashed line). Also shown is the model output for a model when velocity equals the measured flow velocity (0.057 m y^{-1} , (dash-dot line). Both the corrected pH data (filled circles) and measured chemistry for several years (open circles) are displayed.

from the model tuned to fit the 250 ka profile mineralogy (previous section), current values for pCO_2 and temperature, and two different values for v_a ($v_a = v = 0.057 \text{ m y}^{-1}$ or $v_a = 0.016 \text{ m y}^{-1}$). These models were run for 150 y (to ensure that a steady-state was reached with respect to solution chemistry). The model with $v_a = 0.016 \text{ m y}^{-1}$, the same value used in the best-fit mineralogy model for 250 ka, best matched the measured pore water concentrations for alkalinity, pH, Na, and SiO_2 (Fig. 9). Thus, with current pCO_2 and temperature conditions, the model did an even better job of matching measured pore water chemistry.

4.5. Davis Run best-fit model

To model Davis Run model, we followed the approach learned from modeling the Merced data. In the best-fit model, v_a is $\sim 70\%$ of v and $A_{r,m}^o$ for plagioclase was reduced by a factor of ~ 50 relative to $A_{B,m}^o$ (Table 6 and Fig. 10). The $A_{r,m}^o$ values for muscovite and k -feldspar were reduced by more than two orders of magnitude relative to $A_{B,m}^o$ to

approximate the slope of the potassium reaction front in the soil and saprolite (Table 6). Nonetheless, the model underpredicts potassium loss because it predicts no muscovite or k -feldspar dissolution at depths $>10 \text{ m}$ (Fig. 10). As with the Merced 3000 ka profile, when k_{kaol} is reduced by 4–5 orders of magnitude relative to experimental values, then v_a is approximately equal to v_m . But with those parameters, the model underpredicts k -feldspar dissolution by an even greater amount.

4.6. Best-fit model sensitivity

As was the case for the Merced baseline model, varying the values for dispersion, the diffusion coefficient, γ (Eq. (7)), and H from 1% to 99% in the best-fit model had little effect on results at the low flow velocity conditions seen at Merced. In contrast, best-fit model predictions for both sites responded most strongly to the form of the rate law (TST versus sigmoidal or Al-inhibition), choice of v_a , pCO_2 , and temperature, as well as saturated versus

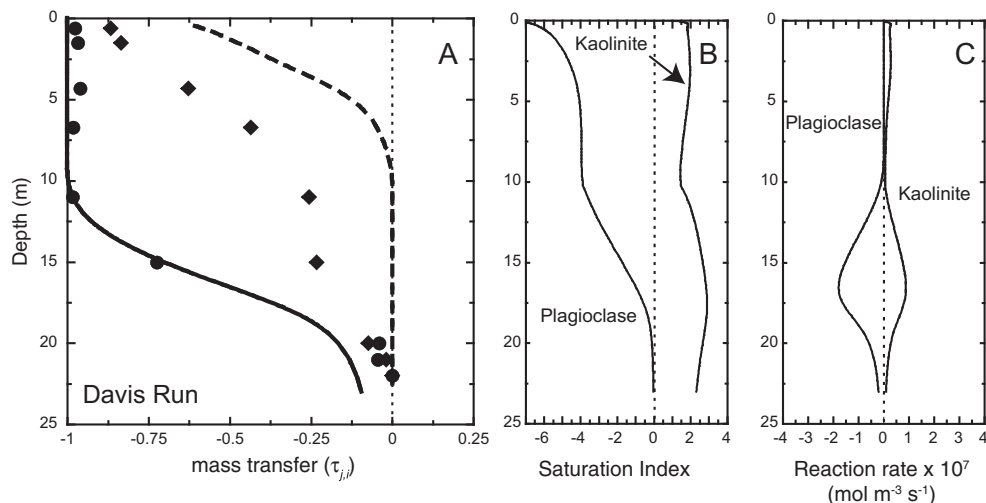


Fig. 10. Best-fit model for 800 ka Davis Run profile. (A) Profiles of $\tau_{j,i}$ for model output for plagioclase (solid line) and k -feldspar (dashed line) plotted along with observed values for plagioclase (circles) and k -feldspar (diamonds). (B) Profiles for saturation indices calculated for plagioclase and kaolinite. (C) Profiles for plagioclase and kaolinite reaction rates per m^3 of porous medium. In all figures, dotted lines delineate 0.

unsaturated flow and k_{kaol} . For example, when the best-fit model was run with a sigmoidal dissolution or Al-inhibition law, the value of $A_{r,plag}^o$ was one order of magnitude higher (and thus closer to $A_{B,plag}^o$) than the $A_{r,plag}^o$ value for a best-fit model with a TST-like rate law (Table 6 and Fig. 11). In addition, use of the Al-inhibition rate law resulted in a different plagioclase front shape than observed for models with TST and sigmoidal rate laws (Table 6 and Fig. 11).

Model sensitivity is higher for Davis Run where dissolution rates are faster than those at Merced. Predicted Z_{plag}^{mid} varies as a function of flow velocity (Fig. 12A and D). A $\pm 5^\circ\text{C}$ variation in model temperature affected L_{plag} in a manner similar in extent to changes in $A_{r,plag}^o$ by $\pm 35\%$ (Fig. 12B and E). This is because changes in temperature result in changes to k_{plag} . Changes to k_{kaol} (Fig. 12C and F) or $p\text{CO}_2$ (not shown) primarily affect Z_{plag}^{mid} while producing minimal changes in L_{plag} .

5. DISCUSSION

5.1. Controls on depth of the reaction front

We find that mineral solubility and the approach to local equilibrium across the reaction fronts are the key factors controlling ω_m and Z_{plag}^{mid} . For example, although the rate constants for plagioclase and k -feldspar dissolution are similar (Table 5; White and Brantley, 2003), k -feldspar is less soluble than plagioclase. This solubility difference explains why Z_{plag}^{mid} values are observed to be deeper in profiles than Z_{kf}^{mid} (this study, White et al., 2001, 2008; Maher et al., 2009). Additionally, the relative insolubility of quartz explains lack of dissolution observed in the field at Merced (White et al., 1996) and model prediction of minimal quartz dissolution in the baseline and other models.

Within the context of our models for weathering profiles, the approach to local equilibrium with respect to a particular mineral was affected by the chemical composition

of the reacting solution. The chemistry of the reacting solution was in turn controlled by three factors: (1) saturated versus unsaturated hydrologic flow, (2) secondary mineral precipitation rates, and (3) fluid flow velocity. Each factor influences the point at which solutions reached chemical equilibrium with respect to dissolving minerals and thus the rate of reaction front advance and mineral depletion. Without the approach to chemical equilibrium, reaction fronts do not have a sigmoidal shape across the depth intervals of interest but rather are nearly vertical, similar to the plagioclase reaction front in the 3000 ka Merced soil (Fig. 8B).

The first factor controlling ω_m was H . Models run with $H = 100\%$ or $H < 100\%$ predicted different solution chemistries and values for Z_{plag}^{mid} and Z_{kf}^{mid} (Fig. 6A and C). With $H = 100\%$, $[\text{CO}_{2(aq)}]$ decreased across L_{plag} with a corresponding increase in $[\text{HCO}_3^-]$ (Fig. 6E). However, the model total alkalinity remained constant (Fig. 6E) because the system was essentially closed with respect to $\text{CO}_{2(g)}$ due to the relatively slow rates of gas diffusion in water. The pH increased across the reaction front and was controlled primarily by mineral dissolution reactions (Fig. 6B). Therefore, in the hydrologically saturated models, relatively high pH values and slow dissolution rates below Z_{mid} were predicted (Fig. 6B and D) and chemical saturation with respect to plagioclase was rapidly approached. The model run with $H = 100\%$ predicted that one meter below Z_{plag}^{mid} , the plagioclase SI increased by a factor of 3440 and dissolution rates decreased by a factor of 570 (Fig. 6C and D). This quick decrease in dissolution rate yielded a plagioclase reaction front that resembles a step function (Fig. 8A).

In contrast, in the model where H was $< 100\%$, $\text{CO}_{2(g)}$ diffusion from the upper boundary was relatively rapid through air in the unsaturated pore space and so $[\text{CO}_{2(aq)}]$ remains constant with depth (Fig. 6E). At higher $[\text{CO}_{2(g)}]$, the model pore fluid was predicted to have lower pH across the reaction fronts in the unsaturated model (Fig. 6B). As a

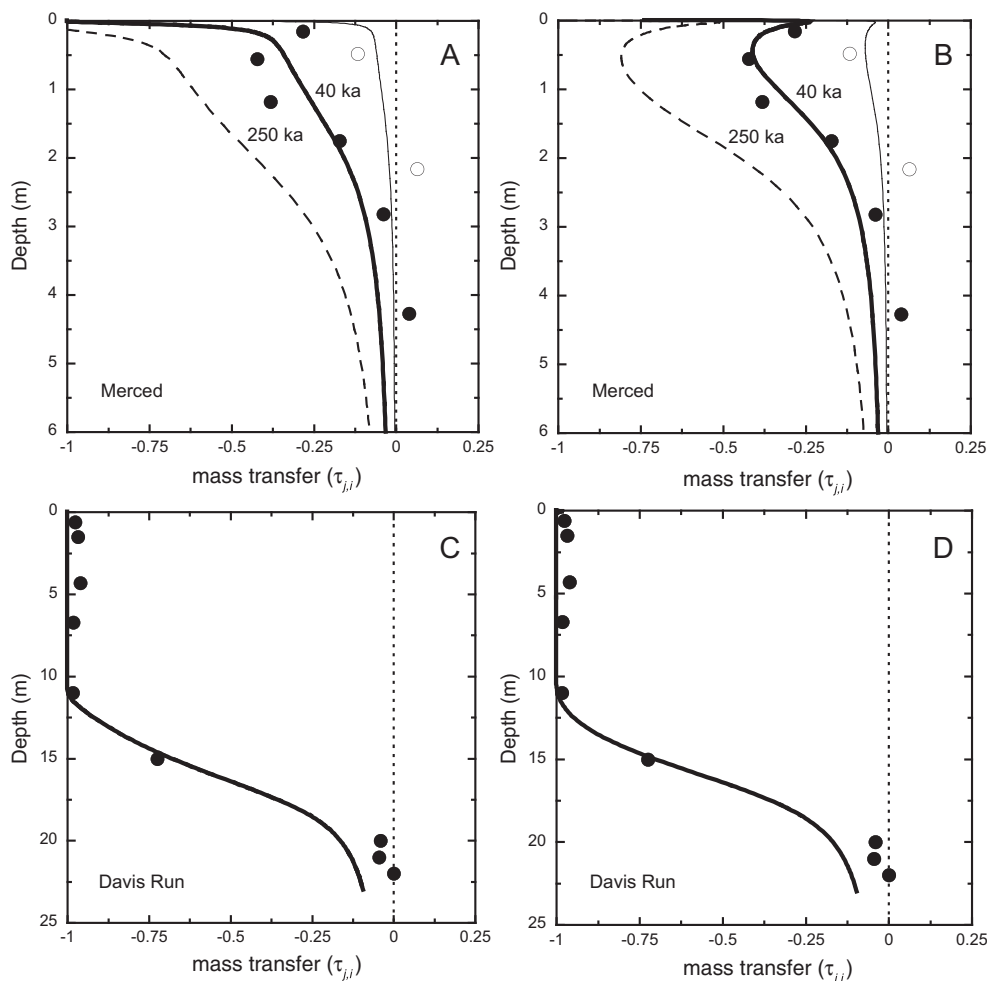


Fig. 11. Best-fit models for Davis Run with sigmoidal or Al-inhibition rate laws. Models run with a sigmoidal rate law are plotted versus depth for (A) Merced at 250 ka for plagioclase (40 ka — thin solid line, 250 ka — thick solid line, 600 ka — dashed line, 3000 ka front is >6 m depth). Observations are also shown for plagioclase (40 ka open circles, 250 ka filled circles). (C) Profiles for Davis Run plagioclase (model output as solid line, using sigmoidal rate equation; observations as circles). Output from models run with an Al-inhibition rate law are shown in (B) for Merced at 250 ka and (D) for Davis Run at 800 ka.

result, the pH increase was smaller across the reaction front because of the constant $[\text{CO}_{2(\text{g})}]$ in the regolith. At these higher $[\text{CO}_{2(\text{g})}]$ and lower pH conditions, the model predicted that one meter below $Z_{\text{plag}}^{\text{mid}}$, the plagioclase SI increased by a factor of 18 and dissolution rates decreased by a factor of 14, a much slower rate of change than for the model with $H = 100\%$ (Fig. 6C and D). The more gradual decrease in reaction rates resulted in a plagioclase front that was almost horizontal across most of the front (to $\tau_{\text{plag},q} \approx -0.25$) (Fig. 6A). Thus the model predicts faster rates of dissolution at the base of the plagioclase reaction front and a faster ω_{plag} (Fig. 6D). When H was <100%, predictions for the 250 ka soil displayed a better match with the observed pH (Figs. 6B and 9A), kaolinite SI (Fig. 6C, field SI = 1–2), and vertical separation of $Z_{\text{plag}}^{\text{mid}}$ and $Z_{\text{kf}}^{\text{mid}}$ (Fig. 6C).

Both plagioclase and k -feldspar Z_{mid} were predicted to be shallower when $H = 100\%$ for Merced (Fig. 6A and C). Additionally, plagioclase and k -feldspar fronts were predicted to be adjacent and located where $\text{CO}_{2(\text{aq})}$ was

depleted (solid line in Fig. 6C; indicated by the two high values in the kaolinite SI). When H was <100%, the predicted plagioclase and k -feldspar fronts were no longer adjacent, which better matches the observed (light dashed line in Fig. 6C). These differences between hydrologically saturated and unsaturated models indicate that front advance rates and front behavior for different minerals is likely to be different between more open systems like those modeled here and closed aquifer systems (e.g., Zhu, 2005). This difference between saturated and unsaturated flow models likely explains why we successfully modeled the plagioclase reaction front at Davis Run, which is located deep in the profile where $H = 100\%$, but we could not successfully model the k -feldspar reaction front, which is located shallower in the profile where H was <100%.

The second key factor controlling ω_m was secondary mineral precipitation rates (and solubility). The importance of the connection between primary mineral dissolution and secondary mineral precipitation has been increasingly highlighted in recent laboratory and modeling studies

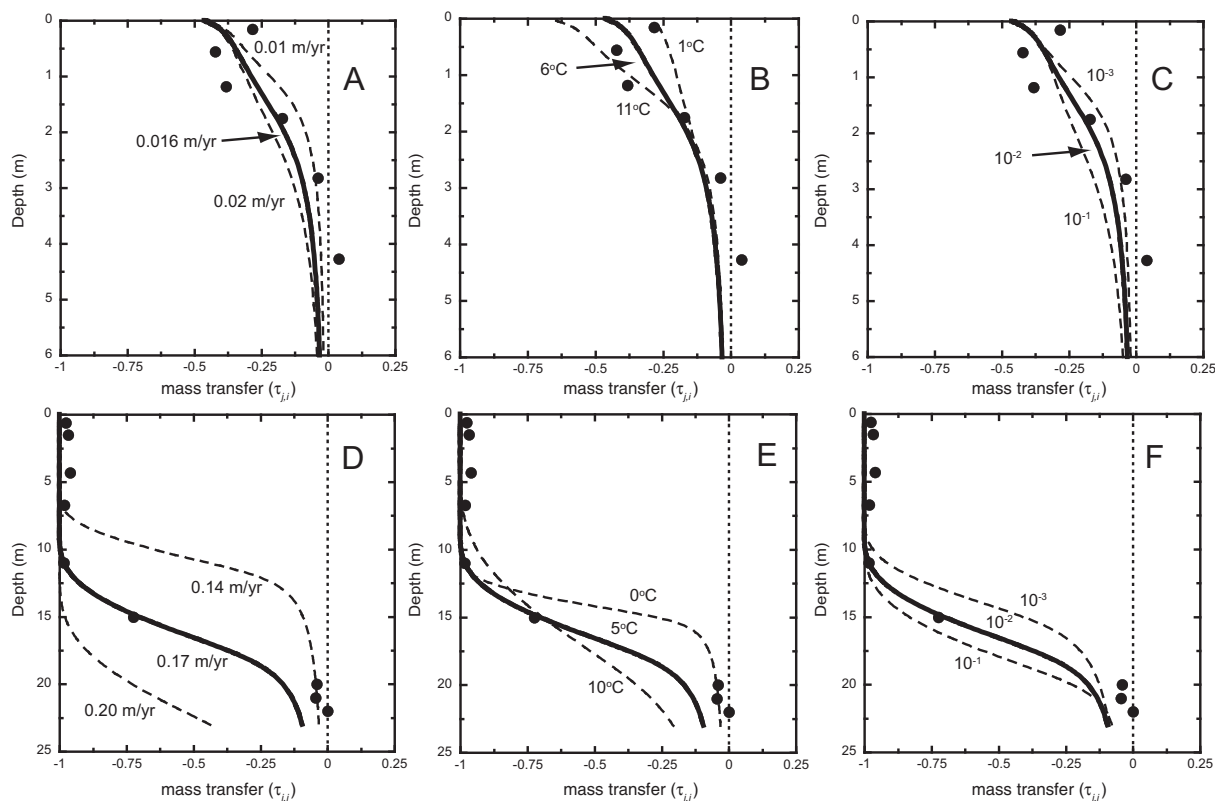


Fig. 12. Sensitivity of best-fit models for Merced and Davis Run. Model-predicted plagioclase reaction fronts are shown based on different assumed values of the fluid flow velocity for (A) Merced at 250 ka and (D) Davis Run at 800 ka; different assumed values of temperature (B) for Merced at 250 ka and (E) Davis Run at 800 ka. Model output based on different values for k_{kaol} for (C) Merced at 250 ka and (F) for Davis Run at 800 ka. Best fit model results are solid lines, variations are dashed lines, and observations are circles. Variations in pCO_2 ($\log pCO_2$ (atm) = -2.1 or -2.5) result in model-predicted fronts similar to those resulting from flow velocity variations (see, for example, similar sensitivity tests in Fig. 5).

(Zhu et al., 2004; Godderis et al., 2006; Godd eris et al., 2010; Ganor et al., 2007; Maher et al., 2009; Zhu and Lu, 2009). The precipitation of secondary minerals serves as a sink for mineral dissolution products. Without that sink, pore water solutions rapidly approach chemical equilibrium. As a result, mineral dissolution rates slow significantly and prevent further advance of the reaction front until a chemically unsaturated parcel of water flows past. In the absence of secondary mineral precipitation, the rapid approach to chemical equilibrium results in extremely low values for ω_m (this study; Ganor et al., 2007; Maher et al., 2009) and thus predicted Z_{plag}^{mid} values shallower than observed (Fig. 5A).

In the only similar study to date, k_{kaol} was reduced by six orders of magnitude relative to the laboratory value in order to set $v_a \approx v$ (Maher et al., 2009). However, as described above, we found reducing k_{kaol} by two orders of magnitude relative to laboratory values (Table 5), along with reducing v_a relative to v , was necessary to achieve a good match to mineral profiles and the pore fluid chemistry. Additionally, all the models reported above were run with $\log K$ for kaolinite set to the discussed values, but in sensitivity testing we found that kaolinite solubility also affected the advance rate of the plagioclase reaction front. More soluble kaolinite results in more dissolution products remaining in solution

and thus produced a similar effect on the advance rate as smaller values of k_{kaol} . Maher et al. (2009) also observed this phenomenon. While a smaller k_{kaol} or higher kaolinite solubility resulted in a factor of two decrease in dissolution rates across the main part of the plagioclase reaction front, the most important effect of varying the kaolinite rate constant or solubility is seen in the predicted ω_{plag} (Fig. 6D). Those same changes in k_{kaol} or $\log K$ for kaolinite resulted in different predictions for solution chemistry profiles, particularly for kaolinite SI values (Fig. 6C). Thus good thermodynamic data for secondary minerals is an essential part of modeling these systems. Additionally, these results suggest that Eq. (5b) is not entirely applicable to multiple-mineral, multiple-component systems since secondary mineral precipitation rates affect ω_m .

The third factor controlling ω_m was v_a . Faster v_a resulted in faster ω_m and thus deeper Z_m^{mid} (Fig. 5B). Once the hydrologic saturation state and secondary mineral parameters were established, v_a was tuned until the predicted reaction front depth matched the observed.

5.2. Controls on slope (or thickness) of the reaction front

When all else is equal, thinner reaction fronts with shallower slopes indicate faster rates of dissolution than thicker

fronts with steeper slopes (this study; Lichtner, 1988; Murphy et al., 1998; White, 2002). The primary parameters controlling L_m are $k_m A_{r,m}^o$ and the form of the rate law (Figs. 5 and 11). MAT (an extrinsic factor) serves as an underlying control since k_m varies with temperature. The effect of varying each parameter was more apparent in systems like Davis Run where reaction rates are faster, e.g., a 5 °C temperature change results in a more obvious difference in the slope of the reaction front (Fig. 12B and E). Note that despite faster plagioclase reaction rates at Davis Run compared to Merced (as seen in the smaller adjustment necessary to $A_{r,m}^o$, Table 6), the reaction front is thicker at Davis Run because v (and v_a) are larger, which fits with the relationship predicted by Eq. (5a). As discussed in the introduction, k_m and form of the rate law may be considered to be intrinsic weathering factors that describe individual minerals. Additionally, both experimental data and model output are consistent with decreases in $A_{r,m}$ over the weathering duration – thus surface area is an intrinsic weathering factor although it changes with time in ways that are hard to predict. Results indicate that L_m increases with v_a and decreases with $k_m A_m$ and thus the general relationship described in Eq. (5a) holds for multiple-mineral, multiple component systems (Fig. 13). Because v_a is constrained by both flow velocity measurements and Z_m^{mid} , $k_m A_m$ (Eq. (5a)) is the only term that can be changed in the model to fit the observed L_m . Due to the importance of $k_m A_m$ in controlling L_m , the form of the rate law (TST, aluminum-inhibition, or sigmoidal) determines how much A_m must be adjusted to achieve model predictions that match observed L_m .

As observed in experimental and field dissolution, the specific surface area of a mineral increases with weathering

duration while reactive surface area decreases both on a specific surface area and volumetric surface area basis (White et al., 1996, 2008; White and Brantley, 2003; Wash-ton et al., 2008). This decrease in reactive surface area results in decreasing dissolution rates for progressively older soils at Merced (White et al., 1996, 2005). In our best-fit models, it was necessary to decrease $A_{r,plag}^o$ to forward model soils of increasing age at Merced (Table 6). This modeling is thus consistent with the conclusion that the reactivity of minerals decreases with duration of weathering. A similar suggestion was made based on modeling of plagioclase weathering in deep sea sediments (Maher et al., 2006) as well as laboratory dissolution studies with extended durations (White and Brantley, 2003). While BET measurements of mineral specific surface area are commonly used as a proxy for reactive surface area, efforts to develop a better measure of the reactive surface area of minerals are ongoing across a range of spatial scales (Gautier et al., 2001; Metz et al., 2005; Navarre-Sitchler and Brantley, 2007; Washton et al., 2008). In the interim, using reactive surface area as an adjustable parameter to model field dissolution seems conceptually preferable to changing rate constants.

Reactive surface area is likely to have two components in field systems. One component is the chemically reactive surface area, which is intrinsic to the mineral and will decline with weathering duration both on a per mass and per volume of regolith basis. A second component of reactive surface area is the hydrologically-accessible reactive surface area, i.e., the volumetric surface area that is accessible to reacting fluids (see below for further discussion). Variations in hydrologically-accessible surface area, which are transport-controlled, are likely to be larger between

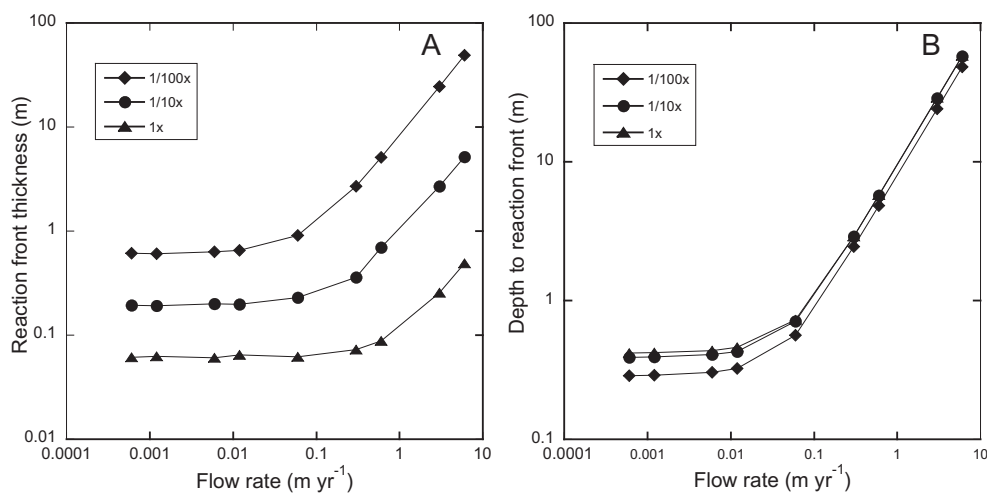


Fig. 13. FLOTTRAN-predicted results for plagioclase: (A) reaction front thicknesses, L_{plag} , and (B) depths, Z_b , plotted versus flow velocity where L_{plag} and Z_b^{plag} are shown as a function of different values for $k_m A_m$. Z_b^{plag} was defined as the value where concentrations returned to 0.99 of the parent plagioclase concentration. Here, Z_b^{plag} was defined as the depth where zero plagioclase remained, and L_{plag} was defined as $Z_b^b - Z_b^l$. Note that the reaction front thickness (A) varies little with flow rate until a critical value of the flow rate where the kinetic-limited regime changes to a mixed regime controlled by both kinetics and transport. The critical value varies with the assumed value of $k_m A_m$ such that the transition between regimes for more reactive phases occurs at higher values of flow rate. Above the critical value, reaction front thickness increases directly with flow rate but inversely with $k_m A_m$ (i.e., compare Eq. (5a)). Similarly, as shown in (B), the depth to the reaction front varies little with flow rate under low-flow conditions ($<0.1 \text{ m yr}^{-1}$) but increases directly with flow rate above that value (compare Eq. (5b)). Under low-flow conditions, transport occurs by both diffusion and advection. These results are for a simplified version of the Merced 250 ka soil where k_m is pH-independent and surface area is constant.

field sites than variations in the chemically-reactive surface area. Thus, a combination of geochemical and hydrological techniques will be necessary to assess reactive surface area in field settings.

5.3. Field versus laboratory

Some of the difficulty in comparing laboratory rate constants with the field is that field-derived rates are apparent rates that incorporate factors such as heterogeneous hydrologic pathways, reactive surface area, and chemical affinity effects (this study; Velbel, 1993; Lichtner and Kang, 2007; Brantley and White, 2009). As a result, it is not surprising that field rates are lower than laboratory rates. For example, previous work using mass balance methods found the difference between plagioclase dissolution rates calculated from field data at Merced (10^{-15} to 10^{-16} mol m⁻² s⁻¹) and Davis Run (10^{-16} to 10^{-17}) versus those measured in the laboratory far from equilibrium at pH 7 ($10^{-12.05}$) to be approximately four orders of magnitude (White et al., 1996, 2001). In contrast, when dissolution was modeled with FLOTRAN using a TST rate law, the difference between $A_{B,m}^o$ and $A_{r,m}^o$ for plagioclase was approximately 55 for Davis Run and 470–1560 for the Merced profiles (Table 6). This smaller difference between laboratory and field when modeling with FLOTRAN suggests that one to two orders of magnitude of the difference in dissolution rates calculated from field data and laboratory dissolution rates is accounted for with a full kinetic rate law that incorporates the slowing of mineral dissolution rates as chemical equilibrium is approached. The Al-inhibition or sigmoidal rate laws further reduced the difference between the field and laboratory to as low as a factor of 5 (Table 6). These results suggest that much of the laboratory-field discrepancy may be explained by dissolution in natural systems predominantly occurring at near-equilibrium conditions (e.g., this study; Kampman et al., 2009; Maher et al., 2009). Thus reactive transport models with full kinetic rate laws are likely to be more accurate for estimating field weathering rates than mass balance approaches to estimating rates. Geometric, analytical, and spreadsheet methods present intermediate approaches, in terms of complexity, to estimating weathering rates.

It is also of interest that model-predicted chemistries of solids and pore water both match field data better when v_a is smaller than v (Table 6 and Fig. 9). Reduction of v_a relative to v was also necessary in a simple spreadsheet model for a similar chronosequence near Santa Cruz, California (White et al., 2008) and in modeling of mineral abundances in Merced A horizons for profiles that weathered 10–3000 ka (Boyle, 2007). In addition, the same v_a value worked best to match both the water and solid chemistry for the Merced 250 ka soil (Figs. 7 and 9).

Based on all these observations, it is apparent that not all the water flowing through the soil encounters reactive mineral surfaces. For instance, slow flow rates, $H < 100\%$ at all depths, and non-isovolumetric weathering in the upper part of the Merced profiles, combined with the higher clay concentrations with soil age due to weathering, increase the likelihood of heterogeneous flow. A hydrological

study performed on the 40 ka Merced soil found that dead-end pores played a major role in solute transport in the soil, particularly in the upper meter (Green et al., 2005).

While, the bromide tracer used by Green et al. (2005) was driven into dead-end pores by high concentration gradients, the opposite effect would occur for weathering products. At Merced, low concentration gradients between the bulk flow and micropores or dead-end pores would result in slow transport out of, and relatively high concentrations of weathering products in, smaller pore spaces. The presence of high-concentration, near-equilibrium fluids in pore spaces provides an explanation of the slow dissolution rates documented in two observational studies. A “nanocatchment” field weathering study found that the best explanation for the correlation of increasing mineral dissolution rates with increasing flow rates was faster transport of solutes from soil micropores (Clow and Drever, 1996). In a laboratory study, mineral dissolution rates were found to be a factor of 4 faster when the same material was dissolved in batch experiments as compared to column experiments with unsaturated fluid flow (Evans and Banwart, 2006). The primary factor causing slower dissolution in the columns was slow rates of transport of solutes between immobile water in the micropores and mobile water flowing through the macropores (Evans and Banwart, 2006). Another climatic and hydrologic factor that may reduce dissolution rates at Merced is the contrasting wet and dry seasons. One laboratory study found that plagioclase dissolution rates decreased after a drying period of 50 days (Ganor et al., 2005). Thus, bulk flow rates measured for soils like Merced, where H is $< 100\%$ and that are seasonally dry, do not represent homogeneous plug flow through the soil column. As a result, the hydrologically-accessible $A_{r,m}$ at Merced is much smaller than the total $A_{r,m}$, which is the likely explanation for the discrepancy of 50–500 (Table 6) that remains even when the Al-inhibition or sigmoidal rate laws are used in the model.

In contrast, at Davis Run, the flow velocities are higher due to higher meteoric precipitation and the lower regolith is at, or near, hydrological saturation (Pavich et al., 1989). The plagioclase reaction front occurs in an isovolumetric weathering system with no compaction and changes in hydrology are minimized with depth in the saprolite and during the period of dissolution (Pavich et al., 1989). For Davis Run, v_a is only reduced by $\sim 30\%$ relative to v (as opposed to a factor of 75–85% for the Merced 250 and 600 ka profiles). The smaller difference between v and v_a may indicate that bulk flow rates are a better measure of mineral-water interaction at Davis Run due to the saturated flow conditions at the depth of mineral reaction.

Despite the hydrological complexities, the model did reasonably well predicting the total amount of clay in the Merced soil profiles but did less well predicting the depth distribution of the clays. Two likely factors, one physical and the other chemical, contribute to the model overprediction of clay concentrations in the shallow subsurface and underprediction of concentrations below about one meter depth. The physical factor is the physical transport and movement of clay particles by water moving through the soil, a process not modeled in FLOTRAN. The chemical

factor is related to the complexation of aluminum with organic matter. Aluminium concentrations were high in the shallow subsurface but declined with depth (White et al., 2005). The decline in aluminum concentration corresponded with a decrease in soil organic matter concentrations (White et al., 2005). Most likely Al and Fe in the upper soil complexed with organic matter. As the organic matter concentration declines, more free aluminum was present in the solution which then precipitated as secondary minerals, a process observed both in forests (Lundström et al., 2000) and in grasslands (Masiello et al., 2004).

5.4. Implications and summary

Model results from this study predict that if all other factors remain constant, higher $p\text{CO}_2$ and temperature will increase geochemical fluxes from a weathering soil system (Fig. 9), especially under hydrologically unsaturated conditions. These observations may be important to understanding effects of anthropogenically-induced climate change on soil systems. Accurate prediction of contemporary fluxes will require more sophisticated hydrological models that include heterogeneous flow and water retention in pores, both of which have been shown to vary with temperature (Richards and Kump, 2003).

We used the reactive transport model FLOTRAN to model mineral dissolution in granitic chronosequence soils (Merced, CA) and granitic saprolite (Davis Run, VA). Our results indicated that depth and fraction of mineral depletion are largely a function of secondary mineral precipitation kinetics and hydrology, including fluid flow velocity and saturated versus unsaturated flow. Once secondary mineral parameters were established, the fraction of mineral remaining in a soil or saprolite was predominantly controlled by fluid flow velocity. Therefore, our approach was (1) properly model the hydrological saturation of the system, (2) reduce the secondary mineral rate constants by two orders of magnitude relative to laboratory constants, and (3) tune fluid flow velocity to a value that correctly predicts the depth at which 50% of the most abundant reactive mineral is depleted. Once the flow velocity is tuned, reaction front slope is modeled by using laboratory rate constants for mineral dissolution and tuning the reactive surface area of minerals in the parent material.

Use of non-TST rate laws reduced the difference between the laboratory and the field at Merced by an order of magnitude. Much of the remaining difference at Merced, where unsaturated hydrologic flow occurred, is likely the result of the heterogeneous flow paths in natural systems as compared to ideal flow paths through porous media – and the implications of these heterogeneities for fluid chemistry. In contrast at Davis Run, where plagioclase weathering occurred in a zone with saturated hydrologic flow, the difference between the laboratory and field was quite small when a sigmoidal rate law was used to model near-equilibrium dissolution. These results strongly indicate that predictions of field mineral dissolution will improve with detailed characterization of the hydrology, particularly in unsaturated flow systems like soils, along with characterization of the geochemistry and mineralogy. Improved

understanding and modeling of heterogeneous flow and transport over geological time scales will be one of the keys to better predicting field mineral dissolution (e.g., Maher, 2010). Dual-continuum reactive transport models (e.g., Lichtner, 2000) will likely be useful to determine the effects of nonhomogeneous flow, e.g., the effect of dead end pores on pore water chemistry and mineral dissolution rates.

Results presented in this paper emphasize that reaction transport models can be used to understand soil mineral weathering over geologic time to 10^6 y using a relatively simplified model with simple modeling of hydrology and that excludes biological effects. The results also suggest that calculating field dissolution rates with a reactive transport model rather than graphical or spreadsheet methods reduces the discrepancy between laboratory rate constants and field-derived rates. In particular, by incorporating secondary mineral precipitation and the approach to chemical equilibrium with respect to soil minerals, either by using TST or sigmoidal rate laws, reactive transport models more closely approximate chemical processes occurring in soil solutions and bridge a major gap between the far-from-equilibrium conditions under which dissolution experiments are usually conducted and the more concentrated and near-equilibrium conditions that predominate in soils.

ACKNOWLEDGEMENTS

We are grateful to A. Navarre-Sitchler and L. Hausrath for many helpful discussions. Three anonymous reviewers provided detailed and helpful comments that resulted in a much improved manuscript. We thank associate editor Chen Zhu for handling the manuscript. Funding was provided by the National Science Foundation grants DGE-9972759 for the Penn State Biogeochemical Research Initiative for Education BRIE), CHE-0431328 for Center for Environmental Kinetics Analysis, and CHE-0535656 for ChemXSeer as well as the Penn State Geosciences Tait and Ohmoto Fellowships.

APPENDIX A. DEPTH-AVERAGED PROFILE CALCULATION

Several depth profiles were collected at each terrace by auger cores and soil pits (Harden, 1987; White et al., 1996). Data from depth profiles from each terrace, collected at slightly different locations and at different depth intervals (Table EA-1), were used to construct a composite profile for each chronosequence soil with the equation:

$$W_m = \frac{\sum w_m f_d f_s}{\sum f_d f_s} \quad (\text{A.1})$$

where W_m is the composite mineral concentration (weight fraction) for some mineral m over a given interval, w_m is the concentration based on quantitative XRD mineralogy data for a given sample interval, f_d is the fraction of the theoretical composite depth interval represented by the actual sampling interval (e.g., if the composite depth interval is 0–30 cm and a sampling interval for one reported soil profile was 0–15 cm, the mineralogy of that sampling interval would be weighted at 0.5), and f_s is the fraction of the sampling interval contained within the composite depth interval

(e.g., if the composite depth interval is 0–30 cm and a sampling interval for a given soil profile is 0–40 cm, the mineralogy of the interval would be weighted at 0.75). Only one depth profile was collected and analyzed for the 40 ka soil. The composite profiles are tabulated in Table EA-6.

The parent mineralogy and composite profiles were converted to a volume basis for use in, and comparison to, the model calculations. The mass to volume conversion was calculated as:

$$V_m = \frac{W_m / \rho_m}{\sum (w_i / \rho_i)} (1 - \phi) \quad (\text{A.2})$$

where w_i and ρ_i are the weight fraction and the specific density, respectively, for the i th mineral, and ϕ is the soil porosity. The mineral specific densities used in the mass to volume conversion are listed in Table EA-7. The total volume fraction, including porosity, must equal one. For the simplified profiles where biotite and hornblende were excluded, the volume fractions for biotite and hornblende was reallocated to pore space so that the total volume fraction remained equal to one. The composite profiles converted to a volume fraction basis are tabulated in Table EA-8.

APPENDIX B. CALCULATION OF MINERAL- AND GRAIN-SIZE SPECIFIC SURFACE AREA

The geometric specific surface area (S_m^{Geo} , $\text{m}^2 \text{g}^{-1}$) for some grain size class g for a mineral m was calculated using the following equation:

$$S_m^{Geo} = \frac{6}{\rho_m d_g} \quad (\text{B.1})$$

where ρ_m = mineral density (g cm^{-3}) and d_g is the mean diameter (cm) for grain size class g . This equation is based upon the assumption of smooth, spherical particles. Mineral specific densities are listed in Table EA-7.

The S_m^{Geo} was converted to a BET-equivalent specific surface area by multiplying by the roughness factor, i.e., the ratio between the BET specific surface area and the geometric specific surface area (Brantley et al., 1999; Helgeson et al., 1984). Grain-size and mineral type were both used to calculate roughness factors. Grain-size specific roughness factors for the Merced parent material were calculated from the reported average BET measurements for the sand and silt grain size classes from the Post-Modesto and Modesto soils (White et al., 1996). For those two soils, roughness varied linearly with λd_g :

$$\lambda_g = 2137d_g + 37.34, \quad R^2 = 0.976 \quad (\text{B.2})$$

Here, λ_g is the roughness factor for a given grain size class g . See Table EA-9 for slight discrepancies between some of the grain size classes the grain size distribution (Harden, 1987) and the grain size classes measured for BET surface area (White et al., 1996). It was assumed that the mineralogy of each grain size fraction was the same as the bulk mineral composition.

In addition to variations with grain size, different minerals have different roughness factors. For this study, mineral-specific roughness factors were calculated by using

average roughness factors calculated from BET measurements of quartz, plagioclase, and k -feldspar mineral separations from the two youngest Merced soils (White et al., 1996). The sum of the average roughness for each of the three minerals was calculated and when the BET surface area was calculated using the calculated roughness, the calculated BET surface area was within 10% of the BET measured surface area of the 0.05–0.1 cm grain size fraction (see Table EA-10). Thus, the roughness for a given mineral m was calculated as the fraction of the total roughness for all minerals ($f_{\lambda,m}$):

$$f_{\lambda,m} = \frac{\lambda_m}{\sum \lambda_a} \quad (\text{B.3})$$

where λ_m is the roughness for mineral m and $\sum \lambda_a$ is the sum of the average roughness factors for quartz, plagioclase, and k -feldspar. The roughness for mineral m in a given grain size class g was calculated from the product of Eqs. (B.2) and (B.3):

$$\lambda_{m,g} = \lambda_g f_{\lambda,m} \quad (\text{B.4})$$

The BET-equivalent specific surface area for a given grain size class g was calculated from the product of Eqs. (B.1) and (B.4):

$$S_{m,g}^{BET} = \frac{6}{\lambda_m d_g} \lambda_{m,g} \quad (\text{B.5})$$

Once the BET-equivalent specific surface area was calculated for each mineral and each grain size class, the total mineral specific surface area was calculated for each mineral. The total mineral specific surface area was calculated from the sum of the surface areas for all the grain size classes and the weight fraction of the soil for each grain size class:

$$S_m = S_{m,g_1} f_{g_1} + S_{m,g_2} f_{g_2} + \dots + S_{m,g_n} f_{g_n} \quad (\text{B.6})$$

Here, g_1 , g_2 , g_n are different grain size classes, and f is the weight fraction for a given grain size class g_n . Either the geometric or the BET specific surface area can be calculated from this equation. The equations outlined thus far were used with the sand and silt fractions to calculate the total soil specific surface area for the primary minerals. The grain size (sand and silt) fractions were normalized so that the sum of the grain size fractions was equal to one.

APPENDIX C. SUPPLEMENTARY DATA

Supplementary data associated with this article can be found, in the online version, at <http://dx.doi.org/10.1016/j.gca.2012.03.021>.

REFERENCES

- Aeschbach-Hertig W., Stute M., Clark J. F., Reuter R. F. and Schlosser P. (2002) A paleotemperature record derived from dissolved noble gases in groundwater of the Aquia Aquifer (Maryland, USA). *Geochim. Cosmochim. Acta* **66**, 797–817.
- Anderson S. P., Dietrich W. E. and Brimhall G. H. (2002) Weathering profiles, mass-balance analysis, and rates of solute loss: Linkages between weathering and erosion in a small, steep catchment. *Geol. Soc. Am. Bull.* **114**, 1143–1158.

- Baisden W. T., Amundson R., Brenner D. L., Cook A. C., Kendall C. and Harden J. W. (2002) A multiisotope C and N modeling analysis of soil organic matter turnover and transport as a function of soil depth in a California annual grassland soil chronosequence. *Glob. Biogeochem. Cycle* **16**, 1135.
- Bandstra J. Z. and Brantley S. L. (2008) Data fitting techniques with applications to mineral dissolution kinetics. In *Kinetics of Water–Rock Interactions* (eds. S. L. Brantley, J. D. Kubicki, and A. F. White). Springer, New York, pp. 211–257.
- Bandstra J. Z., Buss H. L., Campen R. K., Liermann L. J., Moore J., Hausrath E. M., Navarre-Sitchler A. K., Jang J.-H., and Brantley S. L. (2008) Appendix: Compilation of mineral dissolution rates. In *Kinetics of Water–Rock Interactions* (eds. S. L. Brantley, J. D. Kubicki, and A. F. White). Springer, New York, pp. 737–823.
- Bauer A. and Berger G. (1998) Kaolinite and smectite dissolution rate in high molar KOH solutions at 35° and 80 °C. *Appl. Geochem.* **13**, 905–916.
- Beig M. S. and Lutge A. (2006) Albite dissolution kinetics as a function of distance from equilibrium: Implications for natural feldspar weathering. *Geochim. Cosmochim. Acta* **70**, 1402–1420.
- Bender M. (2003) Climate-biosphere interactions on glacial-interglacial timescales. *Glob. Biogeochem. Cycle* **17**, 1082.
- Berner R. A. (1995) Chemical weathering and its effect on atmospheric CO₂ and climate. In *Chemical Weathering Rates of Silicate Minerals* (eds. A. F. White and S. L. Brantley). pp. 565–583.
- Bormann B. T., Wang D., Bormann F. H., Benoit G., April R. and Snyder M. C. (1998) Rapid, plant-induced weathering in an aggrading experimental ecosystem. *Biogeochemistry* **43**, 129–155.
- Boyle J. F. (2007) Simulating loss of primary silicate minerals from soil due to long-term weathering using Allogen: Comparison with soil chronosequence, lake sediment and river solute flux data. *Geomorphology* **83**, 121–135.
- Brantley S. L. (2004) Reaction kinetics of primary rock-forming minerals under ambient conditions. In *Treatise on Geochemistry (Surface and ground water, weathering, and soils)* (ed. J. I. Drever). Elsevier Pergamon, San Diego, CA, pp. 73–118.
- Brantley S. L. (2008) Kinetics of mineral dissolution. In *Kinetics of Water–Rock Interactions* (eds. S. L. Brantley, J. D. Kubicki and A. F. White). Springer, New York, pp. 151–210.
- Brantley S. L. and White A. F. (2009) Approaches to modeling weathered regolith. In *Thermodynamics and Kinetics of Water–Rock Interaction* (eds. E. H. Oelkers and J. Schott). Mineralogical Society of America; Geochemical Society, Chantilly, VA; St. Louis, MO, pp. 435–484.
- Brantley S. L. and Lebedeva M. (2011) Learning to read the chemistry of regolith to understand the critical zone. *Annu. Rev. Earth Planet. Sci.* **39**, 387–416.
- Brantley S. L., White A. F. and Hodson M. E. (1999) Surface area of primary silicate minerals. In *Growth, Dissolution and Pattern Formation in Geosystems* (eds. B. Jamtveit and P. Meakin). Kluwer Academic Publishers, Dordrecht, Netherlands, pp. 291–326.
- Brantley S. L., Goldhaber M. B. and Ragnarsdottir K. V. (2007) Crossing disciplines and scales to understand the critical zone. *Elements* **3**, 307–319.
- Brantley S. L., Bandstra J., Moore J. and White A. F. (2008) Modelling chemical depletion profiles in regolith. *Geoderma* **145**, 494–504.
- Brimhall G. H., Lewis C. J., Ague J. J., Dietrich W. E., Hampel J., Teague T. and Rix P. (1988) Metal enrichment in bauxites by deposition of chemically mature aeolian dust. *Nature* **333**, 819–824.
- Bromwich D. H., Toracinta E. R., Wei H., Oglesby R. J., Fastook J. L. and Hughes T. J. (2004) Polar MM5 simulations of the winter climate of the Laurentide ice sheet at the LGM. *J. Climate* **17**, 3415–3433.
- Bullen T., Fitzpatrick J. A., White A. F., Schulz M. S., and Vivit D. V. (2004) Calcium stable isotope evidence for three soil calcium pools at a granitoid chronosequence. In *Proceedings of the Eleventh International Symposium on Water–Rock Interaction* (eds. R. Wanty and R. I. Seal). A.A. Balkema Publishers, Philadelphia, pp. 813–817.
- Burch T. E., Nagy K. L. and Lasaga A. C. (1993) Free energy dependence of albite dissolution kinetics at 80 °C and pH 8.8. *Chem. Geol.* **105**, 137–162.
- Cama J., Metz V. and Ganor J. (2002) The effect of pH and temperature on kaolinite dissolution rate under acidic conditions. *Geochim. Cosmochim. Acta* **66**, 3913–3926.
- Carey A. E., Lyons W. B. and Owen J. S. (2005) Significance of landscape age, uplift, and weathering rates to ecosystem development. *Aquat. Geochem.* **11**, 215–239.
- Carroll S. A. and Knauss K. G. (2005) Dependence of labradorite dissolution kinetics on CO_{2(aq)}, Al_(aq), and temperature. *Chem. Geol.* **217**, 213–225.
- Carroll-Webb S. A. and Walther J. V. (1988) A surface complex-reaction model for the pH-dependence of corundum and kaolinite dissolution rates. *Geochim. Cosmochim. Acta* **52**, 2609–2623.
- Cerling T. E. (1999) Stable carbon isotopes in Palaeosol carbonates. *Spec. Publ. Int. Assoc. Sedimentol.* **27**, 43–60.
- Chadwick O. A., Brimhall G. H. and Hendricks D. M. (1990) From a black to a gray box – a mass balance interpretation of pedogenesis. *Geomorphology* **3**, 369–390.
- Clow D. W. and Drever J. I. (1996) Weathering rates as a function of flow through an alpine soil. *Chem. Geol.* **132**, 131–141.
- Crews T. E., Kitayama K., Fownes J. H., Riley R. H., Herbert D. A., Muellerdombos D. and Vitousek P. M. (1995) Changes in soil-phosphorus fractions and ecosystem dynamics across a long chronosequence in Hawaii. *Ecology* **76**, 1407–1424.
- Drever J. I. (1994) The effect of land plants on weathering rates of silicate minerals. *Geochim. Cosmochim. Acta* **58**, 2325–2332.
- Drever J. I. and Stillings L. L. (1997) The role of organic acids in mineral weathering. *Colloid. Surface A* **120**, 167–181.
- Elliott W. C., Savin S. M., Dong H. and Peacor D. R. (1997) A paleoclimate interpretation derived from pedogenic clay minerals from the Piedmont Province, Virginia. *Chem. Geol.* **142**, 201–211.
- Evans K. A. and Banwart S. A. (2006) Rate controls on the chemical weathering of natural polymineralic material. I. Dissolution behaviour of polymineralic assemblages determined using batch and unsaturated column experiments. *Appl. Geochem.* **21**, 352–376.
- Ganor J., Roueff E., Erel Y. and Blum J. D. (2005) The dissolution kinetics of a granite and its minerals – implications for comparison between laboratory and field dissolution rates. *Geochim. Cosmochim. Acta* **69**, 607–621.
- Ganor J., Lu P., Zheng Z. P. and Zhu C. (2007) Bridging the gap between laboratory measurements and field estimations of silicate weathering using simple calculations. *Environ. Geol.* **53**, 599–610.
- Gautier J.-M., Oelkers E. H. and Schott J. (1994) Experimental study of *k*-feldspar dissolution rates as a function of chemical affinity at 150 °C and pH 9. *Geochim. Cosmochim. Acta* **58**, 4549–4560.
- Gautier J. M., Oelkers E. H. and Schott J. (2001) Are quartz dissolution rates proportional to BET surface areas? *Geochim. Cosmochim. Acta* **65**, 1059–1070.

- Godderis Y., Francois L. M., Probst A., Schott J., Moncoulon D., Labat D. and Viville D. (2006) Modelling weathering processes at the catchment scale: The WITCH numerical model. *Geochim. Cosmochim. Acta* **70**, 1128–1147.
- Goddéris Y., Williams J. Z., Schott J., Pollard D. and Brantley S. L. (2010) Time evolution of the mineralogical composition of Mississippi Valley loess over the last 10 kyr: Climate and geochemical modeling. *Geochim. Cosmochim. Acta* **74**, 6357–6374.
- Green C. T., Stonestrom D. A., Bekins B. A., Akstin K. C. and Schulz M. S. (2005) Percolation and transport in a sandy soil under natural gradient conditions. *Water Resour. Res.* **41**, W10414.
- Harden J. W. (1982) A quantitative index of soil development from field descriptions: Examples from a chronosequence in central California. *Geoderma* **28**, 1–28.
- Harden J. W. (1987) *Soils developed on granitic alluvium near Merced, California*. US Geological Survey Bulletin 1590-A, Washington DC.
- Helgeson H. C., Murphy W. M. and Aagaard P. (1984) Thermodynamic and kinetic constraints on reaction rates among minerals and aqueous solutions. II. Rate constants, effective surface area, and the hydrolysis of feldspar. *Geochim. Cosmochim. Acta* **48**, 2405–2432.
- Hellmann R. and Tisserand D. (2006) Dissolution kinetics as a function of the Gibbs free energy of reaction: An experimental study based on albite feldspar. *Geochim. Cosmochim. Acta* **70**, 365–383.
- Hodson M. E., Langan S. J., Kennedy F. M. and Bain D. C. (1998) Variation in soil surface area in a chronosequence of soils from Glen Feshie, Scotland and its implications for mineral weathering rate calculations. *Geoderma* **85**, 1–18.
- Huertas F. J., Chou L. and Wollast R. (1999) Mechanism of kaolinite dissolution at room temperature and pressure. Part II: Kinetic study. *Geochim. Cosmochim. Acta* **63**, 3261–3275.
- Johnson J. W., Oelkers E. H. and Helgeson H. C. (1992) Equilibrium constants calculated with SUPCRT92. *Comput. Geosci.* **18**, 899–947.
- Kampman N., Bickle M., Becker J., Assayag N. and Chapman H. (2009) Feldspar dissolution kinetics and Gibbs free energy dependence in a CO₂-enriched groundwater system, Green River, Utah. *Earth Planet. Sci. Lett.* **284**, 473–488.
- Knauss K. G. and Wolery T. J. (1989) Muscovite dissolution kinetics as a function of pH and time at 70 °C. *Geochim. Cosmochim. Acta* **53**, 1493–1501.
- Kump L. R., Brantley S. L. and Arthur M. A. (2000) Chemical weathering, atmospheric CO₂, and climate. *Annu. Rev. Earth Planet. Sci.* **28**, 611–667.
- Lichtner P. C. (1988) The quasi-stationary state approximation to coupled mass transport and fluid–rock interaction in a porous medium. *Geochim. Cosmochim. Acta* **52**, 143–165.
- Lichtner P. C. (1996) Continuum formulation of multicomponent-multiphase reactive transport. In *Reactive Transport in Porous Media* (eds. P. C. Lichtner, C. I. Steefel, and E. H. Oelkers). Mineralogical Society of America, Washington, DC. pp. 1–81.
- Lichtner P. C. (1998) Modelling reactive flow and transport in natural systems. In *Proceedings of the Rome Seminar on Environmental Geochemistry* (ed. L. Marini). Pacini Editore, Ospedaletto. pp. 5–72.
- Lichtner P. C. (2000) Critique of dual continuum formulations of multicomponent reactive transport in fractured porous media. In *Dynamics of Fluids in Fractured Rock, Geophysical Monograph 122* (eds. B. Faybishenko, P. A. Witherspoon, and S. M. Benson). American Geophysical Union, Washington. pp. 281–298.
- Lichtner P. C. (2007) *FLOTRAN: User's Manual*. Report No. LA-UR-02-2349, Los Alamos National Laboratory, Los Alamos, NM. Version 2.0: LA-CC 02–036. October 26, 2007.
- Lichtner P. C. and Carey J. W. (2006) Incorporating solid solutions in reactive transport equations using a kinetic discrete-composition approach. *Geochim. Cosmochim. Acta* **70**, 1356–1378.
- Lichtner P. C. and Kang Q. (2007) Upscaling pore-scale reactive transport equations using a multiscale continuum formulation. *Water Resour. Res.* **43**, W12S15, <http://dx.doi.org/10.1029/2006WR005664>.
- Lundström U. S., van Breemen N., Bain D. C., van Hees P. A. W., Giesler R., Gustafsson J. P., Ilvesniemi H., Karlton E., Melkerud P. A., Olsson M., Riise G., Wahlberg O., Bergelin A., Bishop K., Finlay R., Jongmans A. G., Magnusson T., Mannerkoski H., Nordgren A., Nyberg L., Starr M. and Tau Strand L. (2000) Advances in understanding the podzolization process resulting from a multidisciplinary study of three coniferous forest soils in the Nordic Countries. *Geoderma* **94**, 335–353.
- Maher K. (2010) The dependence of chemical weathering rates on fluid residence time. *Earth Planet. Sci. Lett.* **294**, 101–110.
- Maher K., Steefel C. I., DePaolo D. J. and Viani B. E. (2006) The mineral dissolution rate conundrum: Insights from reactive transport modeling of U isotopes and pore fluid chemistry in marine sediments. *Geochim. Cosmochim. Acta* **70**, 337–363.
- Maher K., Steefel C. I., White A. F. and Stonestrom D. A. (2009) The role of reaction affinity and secondary minerals in regulating chemical weathering rates at the Santa Cruz Soil Chronosequence, California. *Geochim. Cosmochim. Acta* **73**, 2804–2831.
- Malmström M. E., Destouni G., Banwart S. A. and Strömberg B. H. E. (2000) Resolving the scale-dependence of mineral weathering rates. *Environ. Sci. Technol.* **34**, 1375–1378.
- Masiello C. A., Chadwick O. A., Southon J., Torn M. S. and Harden J. W. (2004) Weathering controls on mechanisms of carbon storage in grassland soils. *Glob. Biogeochem. Cycle* **18**, GB4023.
- May H. M., Kinniburgh D. G., Helmke P. A. and Jackson M. L. (1986) Aqueous dissolution, solubilities and thermodynamic stabilities of common aluminosilicate clay–minerals – kaolinite and smectites. *Geochim. Cosmochim. Acta* **50**, 1667–1677.
- Metz V., Raanan H., Pieper H., Bosbach D. and Ganor J. (2005) Towards the establishment of a reliable proxy for the reactive surface area of smectite. *Geochim. Cosmochim. Acta* **69**, 2581–2591.
- Moore J. (2008) *Biogeochemistry of Granitic Weathering*. Ph.D. The Pennsylvania State University.
- Moulton K. L., West J. and Berner R. A. (2000) Solute flux and mineral mass balance approaches to the quantification of plant effects on silicate weathering. *Am. J. Sci.* **300**, 539–570.
- Murphy S. F., Brantley S. L., Blum A. E., White A. F. and Dong H. (1998) Chemical weathering in a tropical weathershed, Luquillo Mountains, Puerto Rico: II. Rate and mechanism of biotite weathering. *Geochim. Cosmochim. Acta* **62**, 227–243.
- NADP (2008) National Atmospheric Deposition Program (NRSP-3), NADP Program Office, Illinois State Water Survey, 2204 Griffith Dr., Champaign, IL 61820.
- Nagy K. L., Blum A. E. and Lasaga A. C. (1991) Dissolution and precipitation kinetics of kaolinite at 80 °C and pH 3: The dependence on solution and saturation state. *Am. J. Sci.* **291**, 649–686.
- Navarre-Sitchler A. and Brantley S. (2007) Basalt weathering across scales. *Earth Planet. Sci. Lett.* **261**, 321–334.
- Oelkers E. H. (1996) Physical and chemical properties of rocks and fluids for chemical mass transport calculations. In *Reactive Transport in Porous Media* (eds. P. C. Lichtner, C. I. Steefel,

- and E. H. Oelkers). Mineralogical Society of America, Washington, DC, pp. 131–191.
- Oelkers E. H., Schott J. and Devidal J.-L. (1994) The effect of aluminum, pH, and chemical affinity on the rates of aluminosilicate dissolution reactions. *Geochim. Cosmochim. Acta* **58**, 2011–2024.
- Oliva P., Viers J. and Dupre B. (2003) Chemical weathering in granitic environments. *Chem. Geol.* **202**, 225–256.
- Oliva P., Dupre B., Martin F. and Viers J. (2004) The role of trace minerals in chemical weathering in a high-elevation granitic watershed (Estibere, France): chemical and mineralogical evidence. *Geochim. Cosmochim. Acta* **68**, 2223–2243.
- Ortoleva P., Auchmuty G., Chadam J., Hettmer J., Merino E., Moore C. H. and Ripley E. (1986) Redox front propagation and banding modalities. *Physica D* **19**, 334–354.
- Palandri J. L. and Kharaka Y. K. (2004) *A Compilation of Rate Parameters of Water-Mineral Interaction Kinetics for application to Geochemical Modeling. Open File Report 2004-1068*. U.S. Geological Survey, Washington, DC.
- Parkhurst D. L. and Appelo C. A. J. (1999) *User's Guide to PHREEQC* (Version 2). US Geological Survey, Washington, DC.
- Pavich M., Leo G. W., Obermeier S. F. and Estabrook J. R. (1989) *Investigations of the Characteristics, Origin, and Residence Time of the Upland Residual Mantle of the Piedmont of Fairfax County, Virginia: Professional Paper 1352*. US Geological Survey, Washington, DC.
- Pavich M. J. (1986) Processes and rates of saprolite production and erosion on a foliated granitic rock of the Virginia Piedmont. In *Rates of Chemical Weathering of Rocks and Minerals* (eds. S. M. Colman and D. P. Dethier). Academic Press, Orlando, pp. 551–590.
- Pavich M. J., Brown L., Valette-Silver J. N., Klein J. and Middleton R. (1985) ^{10}Be analysis of a Quaternary weathering profile in the Virginia Piedmont. *Geology* **13**, 39–41.
- Pavich M. J., Brown L., Harden J. W., Klein J. and Middleton R. (1986) ^{10}Be distribution in soils from Merced River terraces, California. *Geochim. Cosmochim. Acta* **50**, 1727–1735.
- Richards P. L. and Kump L. R. (2003) Soil pore-water distributions and the temperature feedback of weathering in soils. *Geochim. Cosmochim. Acta* **67**, 3803–3815.
- Seiders V. M., Mixon R. B., Stern T. W., Newell M. F. and Thomas C. B. J. (1975) Age of plutonism and tectonism and a new minimum age limit on the Glenarm series in the northeast Virginia Piedmont near Occoquan. *Am. J. Sci.* **275**, 481–499.
- Shiraki R. and Brantley S. L. (1995) Kinetics of near-equilibrium calcite precipitation at 100 °C: An evaluation of elementary reaction-based and affinity-based laws. *Geochim. Cosmochim. Acta* **59**, 1457–1471.
- Stillings L. L., Drever J. I., Brantley S. L., Sun Y. and Oxburgh R. (1996) Rates of feldspar dissolution at pH 3–7 with 0–8 mM oxalic acid. *Chem. Geol.* **132**, 79–89.
- Taylor A. S., Blum J. D. and Lasaga A. C. (2000) The dependence of labradorite dissolution and Sr isotope release rates on solution saturation state. *Geochim. Cosmochim. Acta* **64**, 2389–2400.
- Velbel M. A. (1993) Constancy of silicate-mineral weathering rate-ratios between natural and experimental weathering: implications for hydrologic control of differences in absolute rates. *Chem. Geol.* **105**, 89–99.
- Washton N. M., Brantley S. L. and Mueller K. T. (2008) Probing the molecular-level control of aluminosilicate dissolution: A sensitive solid-state NMR proxy for reactive surface area. *Geochim. Cosmochim. Acta* **72**, 5949–5961.
- White A. F. (2002) Determining mineral weathering rates based on solid and solute weathering gradients and velocities: application to biotite weathering in saprolites. *Chem. Geol.* **190**, 69–89.
- White A. F. and Brantley S. L. (2003) The effect of time on the weathering of silicate minerals: why do weathering rates differ in the laboratory and field? *Chem. Geol.* **202**, 479–506.
- White A. F., Blum A. E., Schulz M. S., Bullen T. D., Harden J. W. and Peterson M. L. (1996) Chemical weathering rates of a soil chronosequence on granitic alluvium: I. Quantification of mineralogical and surface area changes and calculation of primary silicate reaction rates. *Geochim. Cosmochim. Acta* **60**, 2533–2550.
- White A. F., Schulz M. S., Vivit D. V., Blum A. E., Stonestrom D. A. and Harden J. W. (2005) Chemical weathering rates of a soil chronosequence on granitic alluvium: III. Hydrochemical evolution and contemporary mass fluxes and balances. *Geochim. Cosmochim. Acta* **69**, 1975–1996.
- White A. F., Schulz M. S., Vivit D. V., Blum A. E., Stonestrom D. A. and Anderson S. P. (2008) Chemical weathering of a marine terrace chronosequence, Santa Cruz, California I: Interpreting rates and controls based on soil concentration-depth profiles. *Geochim. Cosmochim. Acta* **72**, 36–68.
- White A. F., Blum A. E., Stonestrom D. A., Bullen T. D., Schulz M. S., Huntington T. G. and Peters N. E. (2001) Differential rates of feldspar weathering in granitic regoliths. *Geochim. Cosmochim. Acta* **65**, 847–869.
- White A. F., Schulz M. S., Stonestrom D. A., Vivit D. V., Fitzpatrick J., Bullen T. D., Maher K. and Blum A. E. (2009) Chemical weathering of a marine terrace chronosequence, Santa Cruz, California. Part II: Solute profiles, gradients and the comparisons of contemporary and long-term weathering rates. *Geochim. Cosmochim. Acta* **73**, 2769–2803.
- Williams E. L., Walter L. M., Ku T. C. W., Kling G. W. and Zak D. R. (2003) Effects of CO₂ and nutrient availability on mineral weathering in controlled tree growth experiments. *Glob. Biogeochem. Cycle* **17**, 1041.
- Williams M. R. and Melack J. M. (1997) Atmospheric deposition, mass balances, and processes regulating streamwater solute concentration in mixed-conifer catchments of the Sierra Nevada, California. *Biogeochemistry* **37**, 111–144.
- Wolery T. J. (1992) *EQ3NR, A Computer Program for Geochemical Aqueous Speciation-Solubility Calculations: Theoretical Manual, User's Guide and Related Documentation (Version 7.0)*. UCLR-MA-1110662. Lawrence Livermore National Laboratory, Livermore, CA.
- Yang L. and Steefel C. I. (2008) Kaolinite dissolution and precipitation kinetics at 22 °C and pH 4. *Geochim. Cosmochim. Acta* **72**, 99–116.
- Yokoyama S., Kuroda M. and Sato T. (2005) Atomic force microscopy study of montmorillonite dissolution under highly alkaline conditions. *Clay Clay Miner.* **53**, 147–154.
- Zhu C. (2005) In situ feldspar dissolution rates in an aquifer. *Geochim. Cosmochim. Acta* **69**, 1435–1453.
- Zhu C. and Lu P. (2009) Alkali feldspar dissolution and secondary mineral precipitation in batch systems: 3. Saturation states of product minerals and reaction paths. *Geochim. Cosmochim. Acta* **73**, 3171–3200.
- Zhu C., Blum A. E., and Veblen D. R. (2004) Feldspar dissolution rates and clay precipitation in the Navajo aquifer at Black Mesa, Arizona, USA. In *Proceedings of the Eleventh International Symposium on Water-Rock Interaction* (eds. R. Wanty and R. Seal, II). A. A. Balkema Publishers, Philadelphia, pp. 895–899.